Dirac electrons in quantum rings

L. Gioia, U. Zülicke,* and M. Governale
School of Chemical and Physical Sciences and MacDiarmid Institute for Advanced Materials and Nanotechnology, Victoria University of Wellington, P.O. Box 600, Wellington 6140, New Zealand

R. Winkler
Department of Physics, Northern Illinois University, DeKalb, Illinois 60115, USA and Materials Science Division, Argonne National Laboratory, Argonne, Illinois 60439, USA

(Received 5 January 2018; published 15 May 2018)

We consider quantum rings realized in materials where the dynamics of charge carriers mimics that of two-dimensional (2D) Dirac electrons. A general theoretical description of the ring-subband structure is developed that applies to a range of currently available 2D systems, including graphene, transition-metal dichalcogenides, and narrow-gap semiconductor quantum wells. We employ the scattering-matrix approach to calculate the electronic two-terminal conductance through the ring and investigate how it is affected by Dirac-electron interference. The interplay of pseudospin chirality and hard-wall confinement is found to distinctly affect the geometric phase that is experimentally accessible in mesoscopic-conductance measurements. We derive an effective Hamiltonian for the azimuthal motion of charge carriers in the ring that yields deeper insight into the physical origin of the observed transport effects, including the unique behavior exhibited by the lowest ring subband in the normal and topological (i.e., band-inverted) regimes. Our paper provides a unified approach to characterizing confined Dirac electrons, which can be used to explore the design of valley- and spintronic devices based on quantum interference and the confinement-tunable geometric phase.

DOI: 10.1103/PhysRevB.97.205421

I. INTRODUCTION

Quantum rings [1] are a paradigmatic system for studying topological effects in condensed matter. In particular, coherent electron transport through ballistic rings and similar multiply connected conductors can be used to reveal phenomena associated with geometric phases [2,3], including the Aharonov-Bohm [4–6] and Aharonov-Casher [7–10] effects as well as non-Abelian generalizations [11,12]. Besides the coupling of charge carriers to effective gauge fields, quantum confinement in the ring structure turns out to also importantly affect coherent-electron interference [13–15], which further increases possibilities for its experimental control and application for novel electronic-device functionalities.

Our present paper is motivated by the recent interest in two-dimensional (2D) materials with Dirac-like charge carriers such as single-layer graphene [16–18], single-layer transition-metal dichalcogenides [19,20], and quantum wells in narrow-gap semiconductors [21,22] such as HgTe [23,24] and InAs/GaSb [25,26]. These condensed-matter realizations of 2D Dirac electrons necessarily carry a two-valued flavor degree of freedom [27]. Ring structures in single-layer graphene have previously been studied by analytical and numerical solution of continuum-model-based Dirac equations [28–34] and also numerical tight-binding calculations [32–36]. The bound states in a ring conductor realized in narrow-gap semiconductor quantum wells were also considered [37,38]. Very recently, a theoretical study of quantum rings in MoS_2 has been performed [39]. Experimental realizations have been achieved in HgTe/HgCdTe quantum wells [40], graphene [41–45], and MoS_2 [46].

In contrast to previous theoretical studies that have largely focused on the specifics of various materials systems, we present a broadly applicable and systematic description of the electronic structure and quantum-interference effects in 2D-Dirac-electron quantum-ring conductors based on a completely general subband-$\mathbf{k}\cdot\mathbf{p}$ approach. We obtain an effective Hamiltonian for the azimuthal motion of ring-confined Dirac-like charge carriers that provides deeper insight into characteristic features of the electronic subband structure and allows us to explore physical implications for quantum-transport effects. Complementing existing work that has largely focused on persistent currents in isolated Dirac rings [28–32,38] or studied transport through a particular Dirac-ring realization numerically [34,35], we present analytic results for the two-terminal conductance. In typical experiments [40–45] and previous numerical studies [34,35], the entire structure consisting of the ring conductor and external leads was made out of the same material. This motivated us to discuss in detail the case of flavor-conserving scattering of Dirac electrons at the ring-lead junctions. We identify a purely confinement-induced contribution to the geometric phase, which turns out to have opposite sign for the two flavors of 2D Dirac electrons propagating in the ring. We use this observation to explore possible uses of ring conductors as *flavortronic* devices [47].

The remainder of this paper is organized as follows. We start by introducing the generic model Hamiltonian

*uli.zuelicke@vuw.ac.nz

describing two-flavor 2D-Dirac electrons in a variety of materials in Sec. II. The general subband-$\mathbf{k}\cdot\mathbf{p}$ description of Dirac-electron rings is developed in Sec. III. As part of the derivation, the radial hard-wall-confinement problem for Dirac electrons is solved (Sec. III A) and an effective Hamiltonian for the azimuthal motion of charge carriers in the ring is obtained (Sec. III B). Armed with the understanding of Dirac-ring subband structure, Sec. IV discusses how quantum-interference effects are exhibited in the conductance through the ring. Our scattering-matrix approach is introduced in Sec. IV A, and the fully general two-terminal transmission function for a clean ring with flavor-conserving scattering at the ring-lead junctions is presented. Possible applications of Dirac rings as flavortronics devices are explored in Sec. IV B. We summarize our conclusions in Sec. V, and relevant mathematical details are given in the Appendices.

II. TWO-FLAVOR 2D-DIRAC HAMILTONIAN

The motion of electrons in 2D materials is described by an envelope-function Hamiltonian that can be written in the generic two-flavor 2D-Dirac form [51]

$$H = \begin{pmatrix} \mathcal{H}(\mathbf{k}) & 0 \\ 0 & \mathcal{H}^*(-\mathbf{k}) \end{pmatrix} \equiv \begin{pmatrix} \mathcal{H}^{(+)} & 0 \\ 0 & \mathcal{H}^{(-)} \end{pmatrix}, \tag{1a}$$

$$\mathcal{H}^{(\pm)} = \pm\gamma(k_\pm\,\sigma_- + k_\mp\,\sigma_+) + \frac{\Delta(k)}{2}\,\sigma_3 + \epsilon(k)\,\sigma_0, \tag{1b}$$

where $\sigma_\pm = (\sigma_1 \pm i\,\sigma_2)/2$ are ladder operators for the eigenstates of the diagonal Pauli matrix σ_3 that correspond to the $\mathbf{k} = 0$ conduction and valence-band states, σ_0 is the 2×2 identity matrix, and $k_\pm := k_x \pm i\,k_y$ in terms of Cartesian components of the in-plane wave vector $\mathbf{k} \equiv (k_x, k_y)$. The parameter γ characterizes the interband coupling, and the gap and electron-hole-asymmetry terms are of the general form

$$\Delta(k) = \Delta_0 + \frac{2\gamma}{k_\Delta}\,k^2 \quad , \tag{2a}$$

$$\epsilon(k) = \epsilon_0 + \xi\,\frac{\gamma}{k_\Delta}\,k^2 \quad , \tag{2b}$$

with contributions quadratic in k arising generically due to the influence of remote bands [21,52]. The parameter k_Δ is the wave-vector scale at which remote-band contributions $\propto k^2$ to the gap become comparable to the interband coupling $\propto \gamma k$, and the dimensionless number ξ is a measure of broken electron-hole symmetry. As ϵ_0 constitutes an irrelevant uniform shift in energy, we set $\epsilon_0 = 0$ for convenience. The values of parameters in the Hamiltonian (1b) for specific materials are given in Table I. Systems with $\Delta_0 > 0$ are ordinary, i.e., nontopological, insulators. In contrast, $\Delta_0 < 0$ signifies the band inversion occurring in topological insulators [53].

Switching to polar coordinates $\mathbf{r} = (r,\varphi)$, we take $\mathbf{k} \equiv i\boldsymbol{\nabla}$ to be an operator in real-space representation and note the relation

$$k_\pm = \mathrm{e}^{\pm i\varphi/2}(k_r \pm i\,k_\varphi)\,\mathrm{e}^{\pm i\varphi/2} \quad , \tag{3}$$

with the Hermitian operators [55]

$$k_r = -i\left(\partial_r + \frac{1}{2r}\right) \quad , \tag{4a}$$

$$k_\varphi = -i\,\frac{\partial_\varphi}{r} \quad . \tag{4b}$$

TABLE I. Parameters in the effective 2D-Dirac Hamiltonians for electrons in some representative single-layer (SL) atomic crystals and semiconductor quantum wells (QW).

	γ (eV Å)	Δ_0 (eV)	k_Δ (Å^{-1})	ξ
SL graphene[a]	6.4	$\lesssim$0.01	0.17	0.026
SL MoS_2[b]	3.0	1.7	0.91	0.89
HgTe/CdTe QW[c]	3.7	−0.020	0.053	0.74
InAs/GaSb QW[d]	0.37	−0.016	0.0056	0.088

[a]References [18,54].
[b]Reference [20].
[c]Reference [53], p. 64 (HgTe well width: 7.0 nm).
[d]Reference [53], p. 65 (InAs/GaSb well widths: 10 nm/10 nm).

As the Hamiltonians $\mathcal{H}^{(\pm)}$ commute with total angular momentum $J_z^{(\pm)} = -i\hbar\,\sigma_0\,\partial_\varphi \pm \hbar\,\sigma_3/2$, it is useful to switch to a representation of diagonal $J_z^{(\pm)}$ using the transformation

$$\mathcal{U}_\pm(\varphi) = \exp(\mp i\,\sigma_3\,\varphi/2). \tag{5}$$

It is straightforward to obtain

$$\mathcal{H}^{(\tau)} = \mathcal{U}_\tau(\varphi)\big(\mathcal{H}_r^{(\tau)} + \mathcal{H}_\varphi^{(\tau)}\big)\mathcal{U}_\tau^\dagger(\varphi), \tag{6}$$

where $\tau = \pm$ labels the two flavors of 2D-Dirac electrons, and

$$\mathcal{H}_r^{(\tau)} = \tau\,\gamma\,k_r\,\sigma_1 + \frac{\Delta_0}{2}\,\sigma_3 + \frac{\gamma}{k_\Delta}(\sigma_3 + \xi\,\sigma_0)k_r^2\,, \tag{7a}$$

$$\mathcal{H}_\varphi^{(\tau)} = \gamma\,k_\varphi\,\sigma_2 + \frac{\gamma}{k_\Delta}(\sigma_3 + \xi\,\sigma_0)\left(k_\varphi^2 - \tau\,\sigma_3\,\frac{k_\varphi}{r}\right) \tag{7b}$$

describe their motion in radial and azimuthal coordinates. The expressions (7) form the basis for our further study of quantum states in ring conductors.

III. RING-CONFINED DIRAC ELECTRONS

We assume the ring structure to be defined by an axially symmetric mass confinement [56]

$$H_V = \begin{pmatrix} V(r)\,\sigma_3 & 0 \\ 0 & V(r)\,\sigma_3 \end{pmatrix} \quad . \tag{8}$$

Because of the axial symmetry of the potential $V(r)$, the 2×2 Schrödinger equations

$$[\mathcal{H}^{(\tau)} + V(r)\,\sigma_3]|\Psi^{(\tau)}\rangle = E\,|\Psi^{(\tau)}\rangle \tag{9a}$$

can be written as

$$\mathcal{U}_\tau(\varphi)\big[\mathcal{H}_r^{(\tau)} + \mathcal{H}_\varphi^{(\tau)} + V(r)\,\sigma_3\big]\mathcal{U}_\tau^\dagger(\varphi)\,|\Psi^{(\tau)}\rangle = E\,|\Psi^{(\tau)}\rangle\,, \tag{9b}$$

motivating the separation *Ansatz*

$$|\Psi^{(\tau)}\rangle = \mathrm{e}^{il\varphi}\,\mathcal{U}_\tau(\varphi)\,\frac{1}{\sqrt{2\pi r}}\,\big|\Phi_l^{(\tau)}\big\rangle \quad , \tag{10}$$

where we introduced the azimuthal quantum number l. This transforms Eq. (9b) into the Schrödinger equation for a confined Dirac particle in one spatial dimension [21,57–60],

$$\big[\mathcal{H}_{1\mathrm{D}}^{(\tau)} + V(r)\,\sigma_3 + \mathcal{V}_l^{(\tau)}(r)\big]\big|\Phi_l^{(\tau)}\big\rangle = E_l^{(\tau)}\,\big|\Phi_l^{(\tau)}\big\rangle \quad , \tag{11}$$

with

$$\mathcal{H}_{1D}^{(\tau)} = -i\tau\,\gamma\,\sigma_1\,\frac{d}{dr} + \frac{\Delta_0}{2}\,\sigma_3 - \frac{\gamma}{k_\Delta}(\sigma_3 + \xi\,\sigma_0)\frac{d^2}{dr^2} \quad (12a)$$

and the centrifugal-barrier contribution

$$\mathcal{V}_l^{(\tau)}(r) = \gamma\,\frac{l}{r}\left\{\sigma_2 + \frac{1}{k_\Delta r}[l(\sigma_3 + \xi\,\sigma_0) - \tau(\sigma_0 + \xi\,\sigma_3)]\right\}. \quad (12b)$$

In the spirit of subband-$\mathbf{k}\cdot\mathbf{p}$ theory [61,62], we start by considering Eq. (11) for $l = 0$ [63],

$$\left[\mathcal{H}_{1D}^{(\tau)} + V(r)\,\sigma_3\right]\left|\Phi_0^{(\tau,n)}\right\rangle = E_0^{(\tau,n)}\left|\Phi_0^{(\tau,n)}\right\rangle, \quad (13)$$

and then use the eigenstates $|\Phi_0^{(\tau,n)}\rangle$ as a new basis to calculate the ring-subband dispersions $E_l^{(\tau,n)}$. Here the radial quantum number $n = \pm1, \pm2, \ldots$ labels the ring subbands with the usual convention $E_0^{(\tau,n)} > E_0^{(\tau,n')}$ for $n > n'$. A general eigenstate with $l \neq 0$ is thus expressed as a superposition of basis states,

$$\left|\Phi_l^{(\tau,n)}\right\rangle = \sum_{n'>0}\left(a_{ln'}^{(\tau,n)}\left|\Phi_0^{(\tau,n')}\right\rangle + b_{ln'}^{(\tau,n)}\left|\Phi_0^{(\tau,-n')}\right\rangle\right), \quad (14)$$

with coefficients $a_{ln'}^{(\tau,n)}$ and $b_{ln'}^{(\tau,n)}$ that need to be determined by solving the eigenvalue equation

$$\mathsf{H}_l^{(\tau)}\begin{pmatrix} a_{l1}^{(\tau,n)} \\ b_{l1}^{(\tau,n)} \\ a_{l2}^{(\tau,n)} \\ b_{l2}^{(\tau,n)} \\ \vdots \end{pmatrix} = E_l^{(\tau,n)}\begin{pmatrix} a_{l1}^{(\tau,n)} \\ b_{l1}^{(\tau,n)} \\ a_{l2}^{(\tau,n)} \\ b_{l2}^{(\tau,n)} \\ \vdots \end{pmatrix}, \quad (15)$$

with the new Hamiltonian matrix

$$\mathsf{H}_l^{(\tau)} = \begin{pmatrix} (\mathsf{H}_l^{(\tau)})_{1,1} & (\mathsf{H}_l^{(\tau)})_{1,2} & \cdots \\ (\mathsf{H}_l^{(\tau)})_{2,1} & (\mathsf{H}_l^{(\tau)})_{2,2} & \cdots \\ \vdots & \vdots & \ddots \end{pmatrix} \quad (16a)$$

whose 2×2 sub-blocks are given by

$$(\mathsf{H}_l^{(\tau)})_{n,n'} = \begin{pmatrix} E_0^{(\tau,n)}\delta_{nn'} + \langle\mathcal{V}_l^{(\tau)}(r)\rangle_{n,n'}^{(\tau)} & \langle\mathcal{V}_l^{(\tau)}(r)\rangle_{n,-n'}^{(\tau)} \\ \langle\mathcal{V}_l^{(\tau)}(r)\rangle_{-n,n'}^{(\tau)} & E_0^{(\tau,-n)}\delta_{nn'} + \langle\mathcal{V}_l^{(\tau)}(r)\rangle_{-n,-n'}^{(\tau)} \end{pmatrix}. \quad (16b)$$

Here $\langle\mathcal{O}\rangle_{n,n'}^{(\tau)} \equiv \langle\Phi_0^{(\tau,n)}|\mathcal{O}|\Phi_0^{(\tau,n')}\rangle$ for any operator $\mathcal{O}$, and $\delta_{nn'}$ is the Kronecker symbol.

In the electron-hole-symmetric case (i.e., when $\xi = 0$), the energy-reflection symmetry [64]

$$\sigma_2\left[\mathcal{H}_{1D,\xi=0}^{(\tau)} + V(r)\,\sigma_3\right]\sigma_2 = -\left[\mathcal{H}_{1D,\xi=0}^{(\tau)} + V(r)\,\sigma_3\right] \quad (17)$$

holds, implying the relations

$$E_{0,\xi=0}^{(\tau,-n)} = -E_{0,\xi=0}^{(\tau,n)}\ , \quad (18a)$$

$$\left|\Phi_{0,\xi=0}^{(\tau,-n)}\right\rangle = \sigma_2\left|\Phi_{0,\xi=0}^{(\tau,n)}\right\rangle\ . \quad (18b)$$

As a result, all matrix elements in Eq. (16b) can then be expressed in terms of matrix elements between eigenstates for positive energies with labels $n, n' > 0$,

$$\langle\mathcal{O}\rangle_{n,-n'}^{(\tau)} \xrightarrow{\xi=0} \langle\mathcal{O}\sigma_2\rangle_{n,n'}^{(\tau)}\ , \quad (19a)$$

$$\langle\mathcal{O}\rangle_{-n,n'}^{(\tau)} \xrightarrow{\xi=0} \langle\sigma_2\mathcal{O}\rangle_{n,n'}^{(\tau)}\ , \quad (19b)$$

$$\langle\mathcal{O}\rangle_{-n,-n'}^{(\tau)} \xrightarrow{\xi=0} \langle\sigma_2\mathcal{O}\sigma_2\rangle_{n,n'}^{(\tau)}\ , \quad (19c)$$

which simplifies further calculations.

In general, Eq. (15) can be solved only numerically. It turns out, however, that a hierarchy of relative importance emerges among the 2×2 sub-blocks in Eq. (16a) in the limit of narrow rings, which can be exploited to obtain useful approximate analytical results. We develop this approach in the following using the specific situation of a hard-wall confinement. As a first step, the $l = 0$ eigenstates are determined, as discussed in Sec. III A. We then use these states as basis states for calculating the $l \neq 0$ eigenstates of a hard-wall-confined ring structure according to the procedure outlined formally in Eqs. (14) and (15). Identification of the most important couplings in Eq. (16a) then yields an effective model for the azimuthal motion of ring-confined two-flavor 2D-Dirac electrons given in Sec. III B.

A. Hard-wall-confined quantum ring: $l = 0$ states

To be specific, we now assume a hard-wall potential

$$V(r) = \begin{cases} 0 & \text{for } R - \frac{W}{2} < r < R + \frac{W}{2} \\ \infty & \text{elsewhere} \end{cases}\ , \quad (20)$$

where W and R denote, respectively, the ring's width and average radius. We find the $l = 0$ eigenstates, i.e., solutions of Eq. (13), for this potential by forming a general superposition of same-energy eigenstates of $\mathcal{H}_{1D}^{(\tau)}$ and applying hard-wall boundary conditions at the inner and outer ring radii. See Appendix A for details of the calculation.

Figure 1 illustrates the dependence of the $l = 0$ ring energies on the gap parameter Δ_0, with the latter normalized to the size-quantization energy $E_W = \gamma/W > 0$. Identical energies are obtained for the two series of bound states distinguished by the flavor quantum number $\tau = \pm$. The $n = \pm1$ subbands behave qualitatively differently from the other subbands (those having $|n| > 1$) in that they can lie below the 2D-Dirac gap edges for sufficiently negative values of Δ_0, in which case they correspond to hybridized quantum-spin-Hall edge states [66]. In particular, the energy gap between the lowest conduction ($n = +1$) and highest valence ($n = -1$) subbands vanishes in the limit $-\Delta_0 \gg E_W$. As we will see below, the low-energy electron dynamics in this limit turns out to be

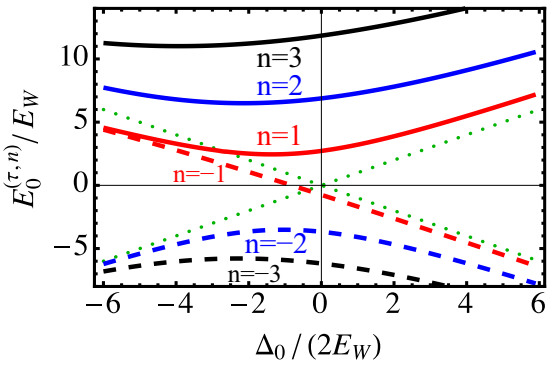

FIG. 1. Spectrum of $l = 0$ bound-state energies for a hard-wall-confined ring structure as a function of the 2D-Dirac gap parameter Δ_0 measured in units of the size-quantization energy $E_W = \gamma/W$. Solid (dashed) red, blue, and black curves correspond to subbands with $n = 1$, 2, and 3 ($n = -1$, -2, and -3), respectively. The thin dotted green lines indicate the position of the 2D-Dirac gap edges $\pm|\Delta_0|/2$. Except for Δ_0, band-structure parameters used in the calculation were fixed at values applicable to a 7-nm HgTe quantum well [65], and we set $k_\Delta W = 26.6$. [For reference, the 7-nm HgTe quantum-well gap satisfies $\Delta_0/(2E_W) = -5.48$.] All energy levels are twofold degenerate in the flavor degree of freedom distinguished by $\tau = \pm$. The $n = \pm 1$ levels lying below the 2D-Dirac gap edges constitute hybridized quantum-spin-Hall edge states.

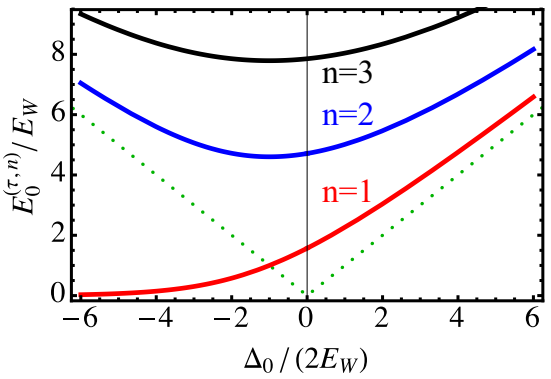

FIG. 2. Spectrum of $l = 0$ bound-state energies for a hard-wall-confined ring structure in the ordinary-Dirac limit [$\Delta(k) = \Delta_0$ and $\epsilon(k) = 0$] as a function of the 2D-Dirac gap parameter Δ_0 measured in units of the size-quantization energy $E_W = \gamma/W$. Red, blue, and black curves correspond to subbands with $n = 1$, 2, and 3, respectively. The dotted lines indicate $E = |\Delta_0|/2$, revealing the evanescent character of the lowest-energy state for $\Delta_0/2 < -E_W$. All levels are twofold degenerate in the flavor quantum number τ.

ultrarelativistic, massless-1D-Dirac-like. In contrast, subbands with $|n| > 1$ have gapped energy dispersions that satisfy $E_0^{(\tau,\pm n)} \gtrless \pm\max\{E_W, |\Delta_0|/2\}$ and therefore exhibit nonrelativistic, ordinary-Schrödinger-like behavior in sufficiently narrow rings for any value of Δ_0.

The situation simplifies considerably in the ordinary-2D-Dirac limit where $\Delta(k) \to \Delta_0$ and $\epsilon(k) \to 0$. Firstly, the subband energies for $l = 0$ become electron-hole-symmetric; i.e., $E_0^{(\tau,n)} = -E_0^{(\tau,-n)}$. Secondly, the bound-state energies measured in units of E_W have a universal dependence on $\Delta_0/(2E_W)$. Figure 2 shows pertinent results for the $n = 1$, 2, and 3 subband states. All energy levels are again twofold degenerate in the flavor quantum number τ. The lowest-subband state becomes evanescent [59] for $\Delta_0/2 < -E_W$, indicating that the system is topological [53]. The fact that the transition to the inverted regime in the quantum-ring system occurs only for sufficiently negative values of the 2D-Dirac gap Δ_0 provides another, particularly clean, example for how size quantization generally competes with the band inversion in topologically nontrivial systems [67,68].

B. Effective Hamiltonian for the azimuthal motion

Having derived the basis states applicable to a hard-wall quantum-ring confinement, the form of the Hamiltonian matrix (16a) can be analyzed in greater detail. The diagonal 2×2 sub-blocks $(\mathsf{H}_l^{(\tau)})_{n,n}$ essentially represent azimuthal dynamics involving only the two subbands labeled by $\pm n$ for fixed $n > 0$. In contrast, the off-diagonal 2×2 sub-blocks $(\mathsf{H}_l^{(\tau)})_{n,n'}$ with $n \neq n'$ embody the coupling between such pairs of subbands. Here we discuss the particular form of both kinds of sub-blocks for hard-wall-confined quantum rings.

A detailed consideration (see Appendix B) motivates the parameterization of diagonal sub-blocks in Eq. (16a) for a hard-wall ring confinement in the general form of a Hamiltonian governing azimuthal motion. It can be written as the sum of two parts,

$$\left(\mathsf{H}_l^{(\tau)}\right)_{n,n} = \left(\mathsf{K}_l^{(\tau)}\right)_{n,n} + \left(\mathsf{L}_l^{(\tau)}\right)_{n,n} \quad , \tag{21}$$

such that the part $(\mathsf{K}_l^{(\tau)})_{n,n}$ contains the most relevant leading terms while corrections, e.g., due to electron-hole asymmetry, are subsumed into $(\mathsf{L}_l^{(\tau)})_{n,n}$. Making the leading dependences on the ring aspect ratio W/R as well as on 2D-Dirac flavor τ and electron-hole asymmetry ξ explicit, we write

$$\left(\mathsf{K}_l^{(\tau)}\right)_{n,n} = -E_W\left(\frac{W}{R}\right)^2 \frac{K_0^{(n)}}{2}\,\tau\, l\,\eta_0 + E_W\,\frac{W}{R}\,K_1^{(n)}\, l\,\eta_1 + \frac{1}{2}\left[E_0^{(\tau,n)} - E_0^{(\tau,-n)}\right]\eta_3 \quad , \tag{22a}$$

$$\left(\mathsf{L}_l^{(\tau)}\right)_{n,n} = \left\{\frac{1}{2}\left[E_0^{(\tau,n)} + E_0^{(\tau,-n)}\right] + E_W\left(\frac{W}{R}\right)^2\left[\frac{\xi\, L_{0\mathrm{A}}^{(n)}}{k_\Delta W}\, l^2 - \frac{L_{0\mathrm{B}}^{(n)}}{k_\Delta W}\,\tau\, l\right]\right\}\eta_0 + E_W\left(\frac{W}{R}\right)^2\left\{\frac{L_{3\mathrm{A}}^{(n)}}{k_\Delta W}\, l^2 - \frac{L_{3\mathrm{B}}^{(n)}}{2}\,\tau\, l\right\}\eta_3. \tag{22b}$$

Here η_j are Pauli matrices acting in the 2×2 subspace where $|\Phi_0^{(\tau,\pm n)}\rangle$ are the basis states, i.e., these states correspond to the eigenstates of η_3 with eigenvalue ± 1. The dimensionless quantities $K_j^{(n)}$ and $L_j^{(n)}$ contain relevant parameter

dependencies and are given most generally in terms of matrix elements as

$$K_0^{(n)} = -\tau \frac{\langle \sigma_2\, W/r\rangle_{n,n}^{(\tau)} + \langle \sigma_2\, W/r\rangle_{-n,-n}^{(\tau)}}{(W/R)^2} \quad , \tag{23a}$$

$$K_1^{(n)} = \frac{\langle \sigma_2\, W/r\rangle_{n,-n}^{(\tau)}}{W/R} \quad , \tag{23b}$$

$$L_{0\mathrm{A}}^{(n)} = \frac{\langle (\sigma_3 + \xi\sigma_0)(W/r)^2\rangle_{n,n}^{(\tau)} + \langle (\sigma_3 + \xi\sigma_0)(W/r)^2\rangle_{-n,-n}^{(\tau)}}{2\xi(W/R)^2}, \tag{23c}$$

$$L_{0\mathrm{B}}^{(n)} = \frac{\langle (\sigma_0 + \xi\sigma_3)(W/r)^2\rangle_{n,n}^{(\tau)} + \langle (\sigma_0 + \xi\sigma_3)(W/r)^2\rangle_{-n,-n}^{(\tau)}}{2(W/R)^2}, \tag{23d}$$

$$L_{3\mathrm{A}}^{(n)} = \frac{\langle (\sigma_3 + \xi\sigma_0)(W/r)^2\rangle_{n,n}^{(\tau)} - \langle (\sigma_3 + \xi\sigma_0)(W/r)^2\rangle_{-n,-n}^{(\tau)}}{2(W/R)^2}, \tag{23e}$$

$$L_{3\mathrm{B}}^{(n)} = \tau \frac{\langle \sigma_2\, W/r\rangle_{-n,-n}^{(\tau)} - \langle \sigma_2\, W/r\rangle_{n,n}^{(\tau)}}{(W/R)^2} + \frac{\langle (\sigma_0 + \xi\sigma_3)(W/r)^2\rangle_{n,n}^{(\tau)} - \langle (\sigma_0 + \xi\sigma_3)(W/r)^2\rangle_{-n,-n}^{(\tau)}}{(W/R)^2}. \tag{23f}$$

More explicit expressions for these are available [69] but, as they are lengthy and unilluminating, we do not present them here. One important feature is that all the functions given in Eqs. (23a)–(23f) remain finite in the limit $W/R \to 0$, i.e., the explicit factors W/R in Eqs. (22a) and (22b) constitute the leading behavior in the limit of narrow rings. The contribution $(\mathsf{L}_l^{(\tau)})_{n,n}$ vanishes in the ordinary-Dirac case where $\Delta(k) \to \Delta_0$, $\epsilon(k) \to 0$, i.e., $k_\Delta W \to \infty$ and $\xi \to 0$. In the same limit, and assuming also a small ring aspect ratio $W/R \to 0$, we obtain

$$K_0^{(n)} \to \frac{1 + \Delta_0/(2E_W)}{\left[E_0^{(\tau,n)}/E_W\right]^2 + \Delta_0/(2E_W)} \quad , \tag{24a}$$

$$K_1^{(n)} \to 1 \quad . \tag{24b}$$

The universal dependence of the quantity $K_0^{(n)}$ on system parameters in this limit is plotted for the three lowest positive-energy subbands in Fig. 3, revealing a qualitatively different behavior of the $n = 1$ subband. In particular, $K_0^{(n)}$ for the higher subbands (i.e., for $n > 1$) vanishes at the point $\Delta_0/2 = -E_W$ where the transition between normal and topological ring-subband structure occurs. The contrasting behavior of $K_0^{(1)}$ is manifested in its opposite monotonicity and absence of any sign change. Understanding the behavior of $K_0^{(n)}$ is relevant because, as discussed in greater detail in Sec. IV, this quantity determines the confinement-induced geometric phase that features prominently in the quantum-interference contribution to the Dirac-ring conductance.

The expression given in Eq. (22a) constitutes the minimal complete model Hamiltonian governing azimuthal motion in a Dirac-electron quantum-ring subband. It becomes accurate

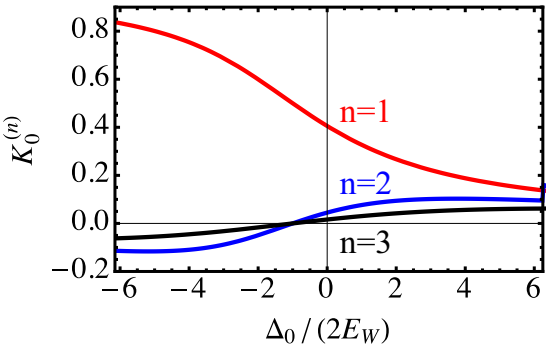

FIG. 3. Universal system-parameter dependence of the quantity $K_0^{(n)}$ for the ordinary-Dirac case [$\Delta(k) \to \Delta_0$, $\epsilon(k) \to 0$] in the narrow-ring limit ($W/R \to 0$) according to Eq. (24a). The red (blue, black) curve shows the result for $n = 1$ (2, 3). Note the qualitatively different behavior of the $n = 1$ subband in the inverted regime where $\Delta_0/2 < -E_W$. All curves for $K_0^{(n)}$ with $n > 1$ cross at the point $(-1,0)$ and exhibit an associated sign change.

in the limit of small electron-hole asymmetry ξ, yielding the approximate subband dispersions

$$E_l^{(\tau,\pm n)} \approx E_W \left\{ -\left(\frac{W}{R}\right)^2 \frac{K_0^{(n)}}{2}\, \tau\, l \pm \sqrt{\left(\frac{E_0^{(\tau,n)}}{E_W}\right)^2 + \left(\frac{W}{R}\right)^2 K_1^{(n)2} l^2} \right\}. \tag{25}$$

The terms $\propto\eta_1$ and $\propto\eta_3$ from Eq. (22a) are the most familiar [28–30,33], as they constitute the expected one-dimensional Dirac form. In particular, the ring confinement induces an effective-gap contribution $\propto\eta_3$ that is generally the largest term, even if the 2D material that hosts the Dirac-ring structure has a vanishing band gap (as is the case, e.g., for graphene). The only possible exception is the lowest ($n = 1$) subband deep in the inverted regime when $\Delta_0/2 \ll -E_W$, as then $E_0^{(\tau,1)} - E_0^{(\tau,-1)} \to 0$. See Figs. 1 and 2 for an illustration. The fact that the size-quantization energy appears like a mass gap in the ring subband energies was implicit in thorough treatments of graphene rings [31,32] but has sometimes been overlooked in simplified models [28–30,33]. The contribution $\propto\eta_0$ embodies the breaking of flavor symmetry due to the ring confinement. For the case of graphene, where the flavor degree of freedom corresponds to electrons from the different valleys $\tau\mathbf{K}$, this was discussed in Refs. [32,34]. Note that, although the term $\propto\eta_0$ is nominally higher order in W/R than the term $\propto\eta_1$, both terms contribute at the same order (quadratic in W/R) to the energy dispersions [cf. Eq. (25)] for finite $E_0^{(\tau,n)} - E_0^{(\tau,-n)}$.

The contributions collected in $(\mathsf{L}_l^{(\tau)})_{n,n}$ [cf. Eq. (22b)] are subleading in the sense that they are proportional to the electron-hole asymmetry ξ or suppressed by the typically small factor $1/(k_\Delta W)$. However, in particular in systems with sizable electron-hole asymmetry as, e.g., HgTe quantum wells, these contributions can become important enough to necessitate their inclusion. In contrast, the coupling between subspaces with different $|n|$ turns out to only marginally affect the low-lying subband dispersions for realistic sets of materials parameters.

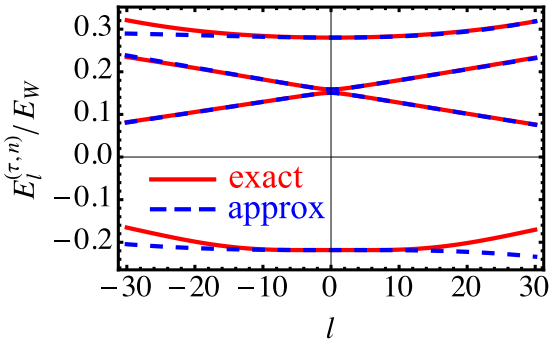

FIG. 4. Comparison of energy dispersions for subbands with $n = \pm 1, \pm 2$ and $\tau = +$ derived from effective Hamiltonians Eq. (21) for individual subbands (dashed blue curves) and the exact spectrum obtained by diagonalizing the full Hamiltonian matrix Eq. (16a) (solid red curves). Results shown were calculated for a ring structure satisfying $k_\Delta W = 26.6$ and $W/R = 0.1$, using band-structure parameters for a 7-nm HgTe quantum well given in Ref. [65].

Figure 4 illustrates the high level of accuracy typically obtained by using only the effective Hamiltonian of Eq. (21) to describe the azimuthal motion of Dirac electrons in the ring structure. Exact and approximate dispersions pertaining to the lowest pair of subbands are seen to be virtually indistinguishable, while deviations become visible for the higher ring subbands.

IV. CONDUCTANCE AND GEOMETRIC PHASE FOR DIRAC-ELECTRON RINGS

To describe electric transport through a quantum ring conductor realized using a 2D-Dirac material, we consider a situation depicted schematically in Fig. 5. Electrons are transmitted from a source lead 1 into a drain lead 2 via the Dirac-ring eigenstates. The coupling of lead modes ν to the eigenmodes of electrons in the ring occurs at the T junctions. To keep the discussion simple, we assume in the following that only the ring subband with label n contributes to transport [70]. The linear electric conductance G is determined by the

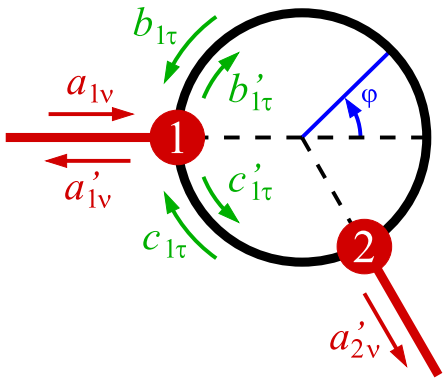

FIG. 5. Electronic transport through a quantum-ring conductor. Leads are connected to the ring at two T junctions from which charge carriers are incoming (outgoing) with amplitude $a_{j\nu}$ ($a'_{j\nu}$) in lead mode ν. Propagation in the ring occurs via confined-Dirac-electron modes having fixed subband index n and flavor $\tau = \pm$. We assume a clean ring, i.e., no scattering to occur between modes except at the junctions.

transmission functions $T_{\nu_2 \leftarrow \nu_1}(E)$ between source-lead and drain-lead modes via [71]

$$G = G_0 \sum_{\nu_1,\nu_2} T_{\nu_2 \leftarrow \nu_1}(E_L) \quad . \tag{26}$$

Here $G_0 \equiv g\, e^2/(2\pi\hbar)$ is the universal quantum of conductance multiplied by a positive integer g counting the degeneracy associated with degrees of freedom that do not affect charge-carrier dynamics and are therefore not included in the model Hamiltonian Eq. (1a) [72], and E_L is the chemical potential in the leads.

The transmission function depends sensitively on details of the device structure, especially on how the leads are coupled to the ring. Two basic physical scenarios can be distinguished according to whether the ring is (i) attached to leads that are made of the same material as the ring, or (ii) attached to a different material (generally via tunneling). Case (i) is more typical nowadays, as it is common to fabricate an entire mesoscopic-conductor system out of a host material using one of many available lithography techniques [73]. In that case, the same two-flavor 2D-Dirac dynamics governs charge-carrier motion in the leads as well as the ring. On the other hand, contact can also be made to a mesoscopic ring structure using scanning-probe tips or other nanoelectronic connections, in which case the charge-carrier dynamics in the leads can be very different from that in the ring. Such case-(ii) scenarios can also be described straightforwardly using the scattering approach to quantum transport. However, as case (ii) is rather uncommon for quantum-ring samples, we consider here only case (i). In particular, given that the general goal in experiments is to make good contacts between the ring and the leads, we assume junctions between the ring and the attached leads to be sufficiently adiabatic so that the flavor (τ) degree of freedom is conserved. This general situation also lends itself to exploring opportunities for *flavortronics*, i.e., quantum-transport effects that capitalize on τ-dependent charge-carrier dynamics. In the context of 2D atomic crystals where τ corresponds to the valley degree of freedom, this concept is generally referred to as *valleytronics* [48].

In our formalism, we allow for the possibility of asymmetric ring structures where the two T junctions with external leads are not identical and/or are not placed diametrically opposite from each other. The ring segments connecting them are assumed to be sufficiently clean so that scattering of charge carriers only occurs at the T junctions. This is a physically realistic assumption as recently fabricated mesoscopic structures of 2D-Dirac materials are ballistic [40,45].

We proceed by presenting the derivation of the transmission functions in Sec. IV A. Our results can be applied to identify features in the conductance that provide direct measures for the peculiar electronic properties of Dirac-electron rings. This is illustrated in greater detail in Sec. IV B, together with implications for using quantum ring conductors as flavor-filtering devices.

A. General transmission function for τ-conserving ballistic ring structures

The procedure for determining the transmission functions $T_{\nu_2 \leftarrow \nu_1}(E)$ through a ring conductor is based on two

fundamental ingredients [5,6]. Firstly, the coupling between lead states and ring states at fixed energy E is embodied by the S matrix [71] of each T junction [74,75]. Secondly, because we assume no scattering to occur in the ring segments connecting the leads, the quantum amplitudes of ring states at different junctions are related simply by the dynamical phases corresponding to propagation of the ring eigenstates between them. These relationships enable the algebraic elimination of ring-state amplitudes, yielding an expression for the outgoing lead-2 amplitudes $a'_{2\nu_2}$ in terms of incoming lead-1 amplitudes $a_{1\nu_1}$ and thus the transmission functions $T_{\nu_2\leftarrow\nu_1}(E) \equiv |a'_{2\nu_2}/a_{1\nu_1}|^2$.

In our situation of interest, charge carriers having different flavor τ are transmitted through the combined leads-and-ring structure completely in parallel. Scattering at the T junctions then occurs only between modes with the same τ,

$$\begin{pmatrix} a'_{j\tau} \\ b'_{j\tau} \\ c'_{j\tau} \end{pmatrix} = \underline{S}_{j\tau} \begin{pmatrix} a_{j\tau} \\ b_{j\tau} \\ c_{j\tau} \end{pmatrix} \quad , \tag{27}$$

and we adopt the most general form for the S matrices,

$$\underline{S}_{j\tau} = \begin{pmatrix} -\sqrt{1-2\varepsilon_{j\tau}}\, e^{i\psi_{j\tau}} & \sqrt{\varepsilon_{j\tau}} & \sqrt{\varepsilon_{j\tau}} \\ \sqrt{\varepsilon_{j\tau}} & \kappa_{j\tau}\, e^{-i\psi_{j\tau}} & \lambda_{j\tau}\, e^{-i\psi_{j\tau}} \\ \sqrt{\varepsilon_{j\tau}} & \lambda_{j\tau}\, e^{-i\psi_{j\tau}} & \kappa_{j\tau}\, e^{-i\psi_{j\tau}} \end{pmatrix}. \tag{28}$$

Here the parameters $\varepsilon_{j\tau}$ with $0 \leqslant \varepsilon_{j\tau} \leqslant 1/2$ are a measure for how strongly lead j is coupled to the ring via mode τ, with $\varepsilon_{j\tau} = 1/2$ ($\varepsilon_{j\tau} = 0$) describing the extremal situation of a fully transparent junction (a completely isolated ring). Scattering of τ-flavor electrons between the ring segments at junction j is described by reflection amplitudes

$$\kappa_{j\tau} = |\kappa_{j\tau}|\, e^{i(\phi_{j\tau}+\varrho_{j\tau})} \tag{29a}$$

and transmission amplitudes

$$\lambda_{j\tau} = |\lambda_{j\tau}|\, e^{i(\phi_{j\tau}-\varrho_{j\tau})} \quad . \tag{29b}$$

The real but otherwise arbitrary phases $\psi_{j\tau}$ are associated with back reflection into the leads. The canonical expression for $\underline{S}_{j\tau}$ given in Eq. (28) covers previously considered special cases of purely real [6,74] or symmetric-beam-splitter [76] T-junction S matrices, as well as the general form given in Ref. [77]. Unitarity of $\underline{S}_{j\tau}$ imposes the relations

$$1 = |\kappa_{j\tau}|^2 + |\lambda_{j\tau}|^2 + \varepsilon_{j\tau} \quad , \tag{30a}$$

$$\varrho_{j\tau} = \frac{s_{j\tau}}{2} \arccos\left(\frac{-\varepsilon_{j\tau}}{2|\kappa_{j\tau}|\,|\lambda_{j\tau}|}\right) \quad , \tag{30b}$$

$$\phi_{j\tau} = \arctan\left[\left|\frac{|\lambda_{j\tau}|-|\kappa_{j\tau}|}{|\lambda_{j\tau}|+|\kappa_{j\tau}|}\right| \tan\varrho_{j\tau}\right] \quad , \tag{30c}$$

with

$$s_{j\tau} = \begin{cases} \mathrm{sgn}(|\lambda_{j\tau}|-|\kappa_{j\tau}|) & \text{if } |\kappa_{j\tau}| \neq |\lambda_{j\tau}|\,, \\ \pm 1 & \text{otherwise}\,. \end{cases} \tag{30d}$$

The relation between quantum amplitudes of ring states at different junctions can be found from the general form of a ring state $|j\tau;\varphi\rangle$ in mode τ emanating from junction j, which is a superposition of counterclockwise-moving and clockwise-moving Dirac-ring eigenstates $|j\tau;\varphi\rangle_\pm$,

$$|j\tau;\varphi\rangle = |j\tau;\varphi\rangle_+ + |j\tau;\varphi\rangle_- \quad , \tag{31a}$$

$$|j\tau;\varphi\rangle_+ = c'_{j\tau}\, e^{il_+^{(\tau)}(\varphi-\varphi_j)}\, \frac{\mathcal{U}_\tau(\varphi-\varphi_j)}{\sqrt{2\pi r}} \left|\Phi_{l_+^{(\tau)}}^{(\tau,n)}\right\rangle, \tag{31b}$$

$$|j\tau;\varphi\rangle_- = -b'_{j\tau}\, e^{il_-^{(\tau)}(\varphi-\varphi_j-2\pi)}\, \frac{\mathcal{U}_\tau(\varphi-\varphi_j)}{\sqrt{2\pi r}} \left|\Phi_{l_-^{(\tau)}}^{(\tau,n)}\right\rangle. \tag{31c}$$

Here φ_j denotes the location of lead j, with the conventions $-\pi \leqslant \varphi_j < \pi$ and $\varphi > \varphi_j$. As shown in Fig. 5, the counterclockwise (clockwise) outgoing mode at junction j propagating in channel τ has amplitude $c'_{j\tau}$ ($b'_{j\tau}$). Due to the ring geometry, the azimuthal angle φ for clockwise-moving partial waves acquires a phase shift 2π with respect to that for counterclockwise-moving partial waves. We used the relation $\mathcal{U}_\tau(\varphi-\varphi_j-2\pi) = -\mathcal{U}_\tau(\varphi-\varphi_j)$ in Eq. (31c). Given E, the azimuthal quantum numbers $l_+^{(\tau)}$ and $l_-^{(\tau)}$ are determined from the relation $E = E_{l_\pm^{(\tau)}}^{(\tau,n)}$ and, by definition, $dE_l^{(\tau,n)}/dl|_{l=l_\pm^{(\tau)}} \gtrless 0$. For the 2D-Dirac-material ring conductors considered here, we have $l_+^{(\tau)} \neq -l_-^{(\tau)}$ in general, but time-reversal symmetry mandates [32]

$$l_\pm^{(\tau)} = -l_\mp^{(-\tau)} \quad . \tag{32}$$

Assuming no scattering to occur within the ring segments between the junctions and considering the situation with $\varphi_2 > \varphi_1$, the form of $|1\tau;\varphi_2\rangle$ ($|2\tau;\varphi_1+2\pi\rangle$) determines how the incoming amplitudes at junction 2 (1) depend on the outgoing amplitudes of junction 1 (2) on the same segment. Using a compact transfer-matrix notation, we can write

$$\begin{pmatrix} c_{2\tau} \\ c'_{2\tau} \end{pmatrix} = e^{i(\theta_\tau-\bar\theta_\tau-\pi)} \begin{pmatrix} e^{-i(\chi-\bar\chi)} & 0 \\ 0 & e^{i(\chi-\bar\chi)} \end{pmatrix} \begin{pmatrix} b'_{1\tau} \\ b_{1\tau} \end{pmatrix}, \tag{33a}$$

$$\begin{pmatrix} c_{1\tau} \\ c'_{1\tau} \end{pmatrix} = e^{-i(\theta_\tau+\bar\theta_\tau)} \begin{pmatrix} e^{i(\chi+\bar\chi)} & 0 \\ 0 & e^{-i(\chi+\bar\chi)} \end{pmatrix} \begin{pmatrix} b'_{2\tau} \\ b_{2\tau} \end{pmatrix}, \tag{33b}$$

in terms of phases

$$\theta_\tau = \tfrac{1}{2}[l_+^{(\tau)} + l_-^{(\tau)}](\varphi_2-\varphi_1-\pi) \quad , \tag{34a}$$

$$\chi = \tfrac{1}{2}[l_+^{(\tau)} - l_-^{(\tau)}](\varphi_2-\varphi_1-\pi) \tag{34b}$$

that depend on the T-junction locations, and the purely electronic-structure-determined phases

$$\bar\theta_\tau = \frac{\pi}{2}[l_+^{(\tau)} + l_-^{(\tau)}] \quad , \tag{35a}$$

$$\bar\chi = \frac{\pi}{2}[l_+^{(\tau)} - l_-^{(\tau)}] \tag{35b}$$

that are intrinsic measures of interference in the Dirac ring. By construction, θ_τ and χ vanish for a symmetric ring structure where $\varphi_2-\varphi_1 \equiv \pi$, and Eq. (32) implies that χ and $\bar\chi$ do not depend on τ whereas $\bar\theta_\tau \equiv \tau\,\bar\theta_+$.

The transmission function for the situation where scattering at the junctions conserves τ can be written as

$T_{\nu_2\leftarrow\nu_1} \equiv T_\tau\,\delta_{\nu_1\tau}\delta_{\nu_2\tau}$, with $T_\tau = |a'_{2\tau}/a_{1\tau}|^2$. A straightforward calculation yields the fully general result

$$T_\tau\big(\chi,\tilde{\chi}_\tau,\theta_{\rm AA}^{(\tau)}\big) = \frac{4\varepsilon_{1\tau}\varepsilon_{2\tau}\big[\cos^2\chi\,\sin^2\tilde{\chi}_\tau\,\cos^2\big(\theta_{\rm AA}^{(\tau)}/2\big)+\sin^2\chi\,\cos^2\tilde{\chi}_\tau\,\sin^2\big(\theta_{\rm AA}^{(\tau)}/2\big)\big]}{\Big||\kappa_{1\tau}||\kappa_{2\tau}|e^{i(\varrho_{1\tau}+\varrho_{2\tau})}\cos(2\chi)+|\lambda_{1\tau}||\lambda_{2\tau}|e^{-i(\varrho_{1\tau}+\varrho_{2\tau})}\cos\theta_{\rm AA}^{(\tau)}-F_\tau(\omega_{1\tau}+\omega_{2\tau},\phi_{1\tau}+\phi_{2\tau},2\tilde{\chi}_\tau)\Big|^2}\,, \tag{36}$$

where

$$F_\tau(\omega,\phi,2\tilde{\chi}) = \frac{1}{2}[e^{i\omega}+\sqrt{(1-2\varepsilon_{1\tau})(1-2\varepsilon_{2\tau})}\,e^{-i\phi}]\cos(2\tilde{\chi}) - \frac{i}{2}[e^{i\omega}-\sqrt{(1-2\varepsilon_{1\tau})(1-2\varepsilon_{2\tau})}\,e^{-i\phi}]\sin(2\tilde{\chi}), \tag{37a}$$

and

$$\theta_{\rm AA}^{(\tau)} \equiv 2\bar{\theta}_\tau + \pi \tag{37b}$$

is the generalized Berry [2], or Aharonov-Anandan [3], phase for an individual τ-conserving transport channel in the Dirac ring. We also used the abbreviations

$$\tilde{\chi}_\tau = \bar{\chi} - \tfrac{1}{2}(\psi_{1\tau}+\psi_{2\tau}-\phi_{1\tau}-\phi_{2\tau}-\omega_{1\tau}-\omega_{2\tau})\,, \tag{37c}$$

$$\omega_{j\tau} = \arg(\lambda_{j\tau}-\kappa_{j\tau})-\phi_{j\tau}\quad, \tag{37d}$$

$$\equiv \arctan\left[\left|\frac{|\lambda_{j\tau}|+|\kappa_{j\tau}|}{|\lambda_{j\tau}|-|\kappa_{j\tau}|}\right|\tan\varrho_{j\tau}\right]\quad. \tag{37e}$$

Among the interesting insights that can be gleaned from Eq. (36) are, firstly, that the phase θ_τ does not appear at all in the expression for T_τ and, secondly, that nonuniversal scattering phases due to the coupling to leads only enter via $\tilde{\chi}_\tau$. In the limit $\chi = 0$ and $\varrho_{j\tau} = \pi/2$, our result Eq. (36) has the form found previously in Ref. [6] for the transmission through a symmetric quantum-ring geometry with real S matrices used to describe the T junctions, and the dependence on χ is consistent with previously considered cases [78,79] of quantum rings with arbitrary location of lead-attachment points.

B. Dirac-ring conductance and τ filtering

For our case of interest where the τ degree of freedom is conserved, we can construct two transport-related quantities of interest. One is the total electric conductance,

$$G = G_0\sum_{\tau=\pm}T_\tau\quad, \tag{38}$$

and the other is the τ polarization of the conductance,

$$P_\tau = \frac{T_\tau - T_{-\tau}}{T_\tau + T_{-\tau}}\quad. \tag{39}$$

In principle, the fully general Eq. (36) for the transmission function T_τ contains all possible τ-dependent effects arising from the coupling to the leads via T junctions, as well as those due to the special features of the Dirac-ring subband structure. In the following, we will focus on discussing the latter and therefore assume that the T-junction parameters are the same for both $\tau = \pm$. To further simplify the discussion, we will consider the case of leads being attached exactly opposite each other ($\varphi_2 - \varphi_1 = \pi$), i.e., $\chi \equiv 0$. Thus the only remaining τ-dependent quantity is the phase $\bar{\theta}_\tau$, and we set $\tilde{\chi}_\tau \equiv \tilde{\chi}$ from now on. It is then instructive to apply the approximate expression Eq. (25) for the nth ring-subband dispersion to determine $l_\pm^{(\tau)}$ and, via Eqs. (35a) and (35b), the phases $\bar{\theta}_\tau$ and $\bar{\chi}$. Considering the case of a narrow ring ($W/R \ll 1$) and $E_{\rm L} - E_0^{(\tau,n)} \ll E_0^{(\tau,n)}$, we find

$$\bar{\theta}_\tau = \tau\,\frac{\pi}{2}\,\frac{E_0^{(\tau,n)}}{E_W}\,\frac{K_0^{(n)}}{\big(K_1^{(n)}\big)^2}\quad, \tag{40a}$$

$$\bar{\chi} = \frac{\pi}{K_1^{(n)}}\sqrt{\frac{2E_0^{(\tau,n)}}{E_W}}\sqrt{\frac{E_{\rm L}-E_0^{(\tau,n)}}{E_W(W/R)^2}}\quad. \tag{40b}$$

Interestingly, $\bar{\theta}_\tau \equiv \tau\,\bar{\theta}_+$ turns out to be determined solely by the Dirac-ring subband structure. As an illustration, Fig. 6 shows a plot of $2\bar{\theta}_+$ that has been calculated from Eq. (40a) for the three lowest subbands in the ordinary 2D-Dirac limit where $\Delta(k) = \Delta_0$ and $\epsilon(k) = 0$. The properties of the curves representing individual subbands can be traced back directly to the behavior of the quantities $E_0^{(\tau,n)}$ and $K_0^{(n)}$ for these subbands that are shown in Figs. 2 and 3, respectively. For example, the confinement-induced geometric phase $\bar{\theta}_\tau$ vanishes for all subbands with $n > 1$ when $\Delta_0/2 = -E_W$ whereas the contribution of the lowest ($n = 1$) remains finite. Furthermore, while the higher subbands recover the ordinary-Schrödinger-electron limit $|2\theta_+| \approx \pi$ when $|\Delta_0| \gg E_W$ both in the normal and topological (i.e., inverted-band) regimes, the geometric phase of the lowest subband approaches the massless-2D-Dirac limit $2\theta_+ = 0$ deep in the topological regime.

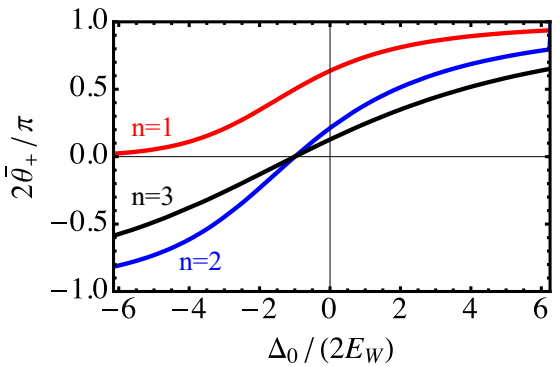

FIG. 6. Electronic-structure-related contribution $2\bar{\theta}_+$ to a Dirac ring's intrinsic Aharonov-Anandan phase that is associated with the $\tau = +$ transport channel. The figure shows this phase for the subband with $n = 1$ (2, 3) as the red (blue, black) curve for a narrow-ring structure in the ordinary-Dirac limit where $\Delta(k) = \Delta_0$ and $\epsilon(k) = 0$ (corresponding, e.g., to single-layer graphene). Note the qualitatively different behavior of the $n = 1$ subband for which $2\bar{\theta}_+ \approx 0$ deep in the inverted regime, whereas $|2\bar{\theta}_+| \approx \pi$ when $|\Delta_0| \gg E_W$ for the higher subbands.

In contrast to $\bar{\theta}_\tau$, $\bar{\chi}$ (and thus also $\tilde{\chi}_\tau \equiv \tilde{\chi}$ here) has a strong dependence on the chemical potential $E_{\rm L}$ in the leads. Given that $\tilde{\chi}$ is renormalized by nonuniversal phase shifts associated with scattering at the T junctions [see Eq. (37c)], features exhibited in the energy dependence of the transmission function will generally be quite sample specific—even if the T-junction S-matrix parameters vary only weakly in the experimentally relevant range of energy.

In addition to adjusting the chemical potential in the leads, application of a perpendicular magnetic field $\mathbf{B}$ can also be used as an experimentally accessible knob to manipulate transport through a ring conductor via Aharonov-Bohm interference [4–6,32]. Formally, the effect of finite $\mathbf{B} \equiv \nabla \times \mathbf{A}$ in a sufficiently narrow ring can be modeled by introducing an infinitesimally thin tube of magnetic flux ψ piercing the ring plane at its origin via the vector potential $\mathbf{A} = [\psi/(2\pi r)]\,\hat{\boldsymbol{\varphi}}$. Making the required substitutions $\mathcal{H}^{(\pm)}(\mathbf{k}) \to \mathcal{H}^{(\pm)}(\mathbf{k} + 2\pi\mathbf{A}/\psi_0)$ in Eq. (1a), with ψ_0 denoting the magnetic flux quantum, translates into the changes $k_\varphi \to k_\varphi + \psi/(\psi_0 r)$ and $\mathcal{V}_l^{(\tau)}(r) \to \mathcal{V}_{l+\psi/\psi_0}^{(\tau)}(r)$. Thus the effect of the magnetic flux is to rigidly shift the quantum-ring dispersions in l by the amount ψ/ψ_0, with the only ramification for the transmission function Eq. (36) being that the Aharonov-Anandan phase becomes flux dependent,

$$\theta_{\rm AA}^{(\tau)} \equiv \theta_{\rm AA}^{(\tau)}(\psi) = 2\bar{\theta}_\tau + 2\pi\left(\frac{1}{2} - \frac{\psi}{\psi_0}\right) \quad , \tag{41}$$

resulting in a ψ_0-periodic modulation of the conductance as a function of flux ψ [5,6]. As $\bar{\theta}_\tau$ is robust with respect to changes in the leads' chemical potential and details of the ring-lead junction morphology, it will be possible to measure its magnitude via the magnetic-field dependence of the conductance. In particular, it will be interesting to map the transition from the nonrelativistic, Schrödinger-like regime $\Delta_0 \gg E_W$ (where $2\bar{\theta}_+ \approx \pi$) to the ultrarelativistic, Dirac-like regime $-\Delta_0 \gg E_W$ (where $2\bar{\theta}_+ \approx 0$) exhibited by the $n = 1$ subband (cf. Fig. 6). In contrast, the higher subbands show nonrelativistic behavior whenever $|\Delta_0| \gg E_W$, regardless of the existence of band inversion.

To illustrate more directly how these distinctive ring-subband properties are manifested in the two-terminal conductance, we consider the situation with fully transparent T junctions, which is realized for $\varepsilon_{j\tau} \equiv 1/2$. As concomitantly $\varrho_{j\tau} = \pm\pi/2$, $\phi_{j\tau} = 0$, $\omega_{j\tau} = \pm\pi/2$, and keeping with the current assumption of a symmetric ring structure where $\chi = 0$ and also $\tilde{\chi}_{j\tau} \equiv \tilde{\chi}$, Eq. (36) specializes to

$$T_\tau^{(\rm tr)}\big(\tilde{\chi}, \theta_{\rm AA}^{(\tau)}\big) = \frac{2\,\sin^2\tilde{\chi}\,\big(1 + \cos\theta_{\rm AA}^{(\tau)}\big)}{\big(\frac{1}{2}\big[1 + \cos\theta_{\rm AA}^{(\tau)}\big] - \cos(2\tilde{\chi})\big)^2 + \sin^2(2\tilde{\chi})} \,. \tag{42}$$

For the purpose of the present discussion, we fix $\sin^2\tilde{\chi} = 1$ for simplicity. Figure 7 shows a density plot of the two-terminal conductance through an ordinary-2D-Dirac ring that could be realized, e.g., in graphene, as a function of applied magnetic flux and the quantity $\Delta_0/(2E_W)$. Results are shown for two cases corresponding to situations where transport occurs via states in the lowest ($n = 1$) and first excited ($n = 2$) ring subband, respectively. The characteristic dependence of the geometric phase on ring-structure parameters is clearly exhibited in the interference-fringe pattern of the conductance. In particular, massless-Dirac (ordinary-Schrödinger) behavior is manifested here by conductance minima occurring for integer (half-integer) values of ψ/ψ_0. The pattern seen for the $n = 1$ subband shows very clearly a transition between these two limiting regimes. In contrast, the $n = 2$ subband (like all other higher-$|n|$ subbands) exhibits an interference pattern indicative of massless-Dirac behavior only in a narrow region around the point where $\Delta_0/2 = -E_W$, which is a direct consequence of the vanishing $K_0^{(n)}$ for $n > 1$ at this special point where the transition between normal and topological ring-subband structures occurs (cf. Fig. 3). For the subband $n = 1$ and

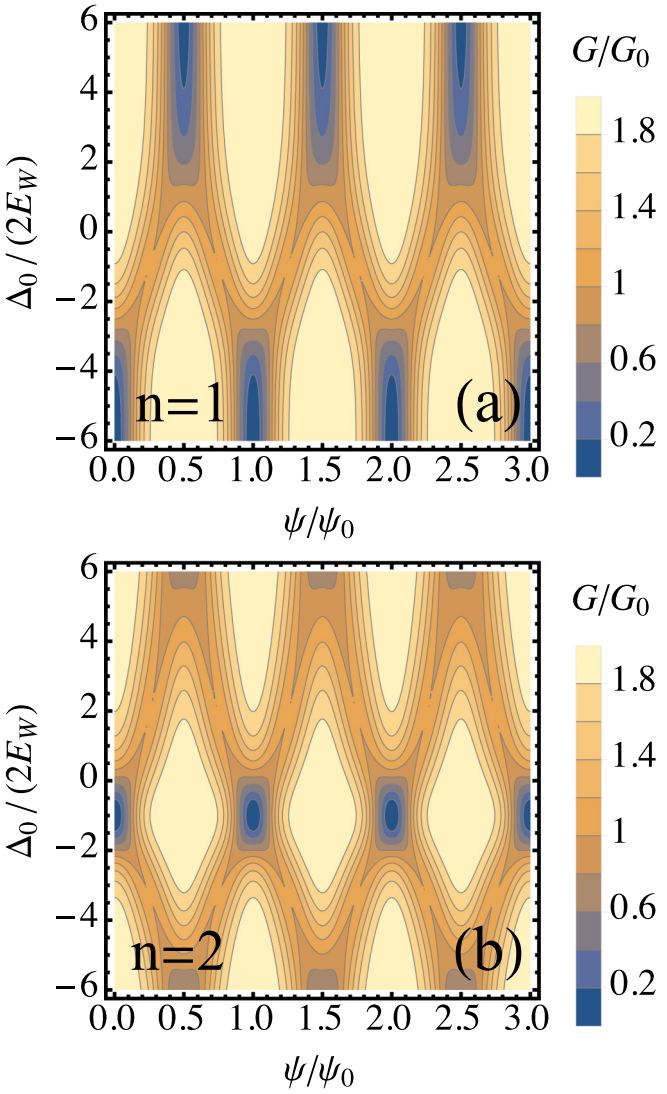

FIG. 7. Two-terminal conductance G through a ring realized in a material where charge-carrier dynamics mimics that of ordinary 2D-Dirac electrons [$\Delta(k) = \Delta_0$, $\epsilon(k) = 0$] contacted to leads via fully transparent T junctions. The density plots show G in units of $G_0 \equiv g\,e^2/(2\pi\hbar)$ as a function of magnetic flux ψ in units of the flux quantum $\psi_0 \equiv 2\pi\hbar/e$ and the parameter combination $\Delta_0/(2E_W)$ characterizing the ring confinement. Results in panel (a) [(b)] were calculated using Eq. (42) for the situation where transport occurs through the $n = 1$ [$n = 2$] subband and assuming $\sin^2\tilde{\chi} = 1$.

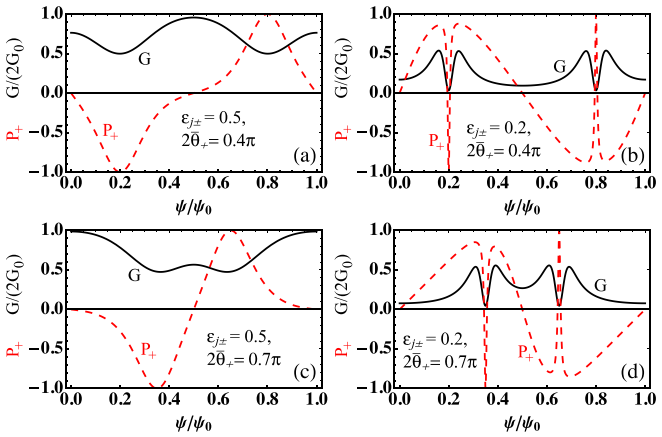

FIG. 8. Dependence of the conductance $G/(2G_0)$ (black solid curves) and τ polarization P_+ (red dashed curves) on magnetic flux ψ for a symmetric ring structure where T-junction S matrices are assumed to be real as, e.g., in Ref. [6]. Here ψ_0 denotes the quantum of magnetic flux. Other parameters used in the calculation are $\sin^2\tilde{\chi}_\pm = 1$, $s_{j\pm} = 1$ $(j = 1,2)$, and $\varepsilon_{j\pm} = 0.5$ [0.2, 0.5, 0.2], $2\bar{\theta}_+ = 0.4\,\pi$ [$0.4\,\pi$, $0.7\,\pi$, $0.7\,\pi$] for panel (a) [(b), (c), (d)].

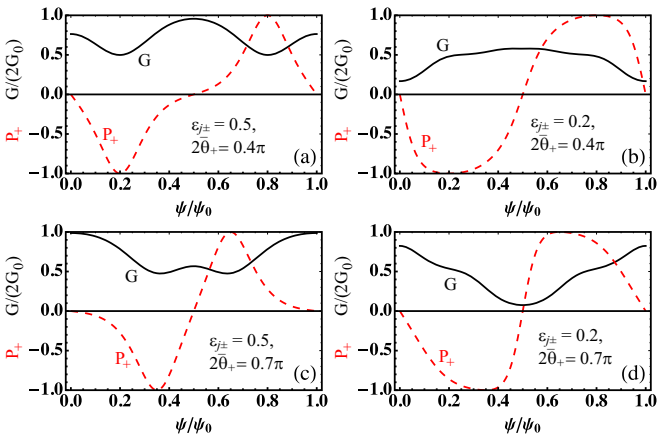

FIG. 9. Dependence of the conductance $G/(2G_0)$ (black solid curves) and τ polarization P_+ (red dashed curves) on magnetic flux ψ (measured in units of the magnetic flux quantum ψ_0) for a symmetric ring structure with beam-splitter-type T-junction S matrices as given, e.g., in Ref. [76]. Other parameters used in the calculation are $\sin^2\tilde{\chi}_\pm = 1$, $s_{j\pm} = 1$ $(j = 1,2)$, and $\varepsilon_{j\pm} = 0.5$ [0.2, 0.5, 0.2], $2\bar{\theta}_+ = 0.4\,\pi$ [$0.4\,\pi$, $0.7\,\pi$, $0.7\,\pi$] for panel (a) [(b), (c), (d)].

$\Delta_0 = 0$, the oscillations of the ring conductance calculated here as a function of magnetic flux agree with numerical results presented in Ref. [34] for graphene rings in the one-mode regime.

Before concluding, we explore the dependence of Dirac-ring interference and flavor filtering on the transparency of the T junctions connecting the ring to external leads. Two special cases are considered according to whether T junctions are described by real S matrices as in Ref. [6] or beam-splitter-type S matrices as in Ref. [76].

Real S matrices describing the ring-lead coupling are obtained from the general expression Eq. (28) by setting $\varrho_{j\tau} = \pi/2$ and $\psi_{j\tau} = 0$ or π. With the additional assumptions $\chi = 0$ and $\varepsilon_{j\tau} \equiv \varepsilon$ for a symmetric ring structure, as well as $\sin^2\tilde{\chi}_\tau = 1$ for simplicity, the transmission function from Eq. (36) specializes to

$$T_\tau^{(\mathrm{re})}\big(\theta_{\mathrm{AA}}^{(\tau)}\big) = \frac{2\varepsilon^2\big(1+\cos\theta_{\mathrm{AA}}^{(\tau)}\big)}{\big[\frac{(\sqrt{1-2\varepsilon}+1)^2}{4}\big(1+\cos\theta_{\mathrm{AA}}^{(\tau)}\big)+\frac{(\sqrt{1-2\varepsilon}-1)^2}{2}\big]^2}. \tag{43}$$

The magnetic-flux dependence of the total Dirac-ring conductance G as well as the flavor (τ) polarization $P_+ \equiv -P_-$ for this situation is illustrated in Fig. 8 for particular parameter values, including examples for fully transparent T junctions ($\varepsilon = 0.5$) and more weakly coupled leads ($\varepsilon = 0.2$). In this case, interference-related minima in G generally coincide with maxima of $|P_+|$. The flux values at which these features occur can be shifted by tuning the confinement-related Aharonov-Anandan angle $\bar{\theta}_+$. Reduced transparency of the contacts with leads results in a precipitous narrowing of their flux-dependence line shape into resonances that are indicative of the isolated-ring bound-state energies [6].

A T junction acting as a beam splitter is described by an S matrix of the form given in Eq. (28) where $|\kappa_{j\tau}| = |\lambda_{j\tau}| \equiv \sqrt{(1-\varepsilon_{j\tau})/2}$. Assuming again $\chi = 0$, $\varepsilon_{j\tau} \equiv \varepsilon$, and $\sin^2\tilde{\chi}_\tau = 1$, Eq. (36) yields

$$T_\tau^{(\mathrm{bs})}\big(\theta_{\mathrm{AA}}^{(\tau)}\big) = \frac{2\varepsilon^2\big(1+\cos\theta_{\mathrm{AA}}^{(\tau)}\big)}{\varepsilon^2\big\{\frac{1}{2}\big[1+\cos\theta_{\mathrm{AA}}^{(\tau)}\big]+1\big\}^2+\frac{1-2\varepsilon}{4}\big[1-\cos\theta_{\mathrm{AA}}^{(\tau)}\big]^2}. \tag{44}$$

Figure 9 shows the magnetic-flux dependence of G and P_+ for this case, using the same values for other parameters as we did for the case of real T-junction S matrices in Fig. 8. Note that, for fully transparent T junctions ($\epsilon_{j\tau} = 1/2$), the cases of real and beam-splitter-type S matrices yield identical results, as is visible from the direct comparison of Figs. 8(a) and 8(c) with Figs. 9(a) and 9(c), respectively. In contrast, for a ring that is weakly connected to leads, the different T-junction types are associated with very different behavior. Unlike the situation with real S matrices, the magnitude of the flavor (τ) polarization of the current is close to unity over a significant range of values for the magnetic flux ψ in the configuration with beam-splitter T junctions. Also in contrast to the real-S-matrix case, the range of flux values for maximum valley polarizations coincides with sizable values of total conductance G. The general location of valley-polarization maxima remains tunable overall by adjusting $\bar{\theta}_+$, but their flux dependence does not exhibit a narrow resonancelike line shape. Quantum-ring structures where T junctions are of beam-splitter type thus lend themselves for use as very effective Dirac-electron-flavor filters.

V. CONCLUSIONS

We have developed a general framework for describing theoretically both the radial quantum confinement and the azimuthal motion of 2D-Dirac-like charge carriers in ring conductors. The formalism applies to a wide range of 2D materials, including narrow-gap semiconductor quantum wells

as well as few-atom-thick crystals, and also covers situations with band inversion. We present a generally valid effective model for the azimuthal motion that illuminates a number of interesting features of the Dirac-quantum-ring subband structure and also yields quantitative expressions for corresponding magnitudes. One such interesting feature is the dependence of subband dispersions on the flavor degree of freedom carried by 2D-Dirac-like charge carriers. Another is the competition between size quantization and band inversion that shifts the topological regime for the quantum-ring system to values of the 2D-Dirac gap Δ_0 that need to satisfy $\Delta_0/2 < -\gamma/W$ in terms of the ring width W and 2D-Dirac-electron Fermi velocity $\gamma/\hbar$. A massless-Dirac-like dispersion can occur for ring-confined charge carriers from the lowest pair of conduction and valence subbands in the limit of large negative 2D-Dirac gap, i.e., when $\Delta_0 < 0$ and $|\Delta_0| \gg 2\gamma/W$. More generically, size-quantization effects ensure that the subband dispersions are gapped, even for the lowest subband, and even when the 2D-Dirac gap vanishes as is the case, e.g., in graphene.

We have used the insight gained from calculated Dirac-ring subband dispersions and eigenstates to investigate quantum-interference effects in the two-terminal conductance. Our analysis is based on the scattering-matrix approach and carefully incorporates effects arising from the coupling to external leads. We obtain a fully general expression for the transmission function [Eq. (36)] for the case where T junctions with the leads conserve the charge carriers' flavor degree of freedom and motion in the ring segments between the leads is ballistic. Our consideration of this situation is motivated by the recent realization of ballistic ring structures in 2D-Dirac materials [40,45]. Properties of the Dirac-ring subband structure turn out to uniquely influence the flavor-dependent geometric (Berry, Aharonov-Anandan) phase $\theta_{\rm AA}^{(\tau)}$, which is also dependent on magnetic flux ψ [as per Eq. (41)] but otherwise entirely robust against nonuniversal, hard-to-determine experimentally, details such as shifts in quantum phases associated with the T junctions and the Fermi energy in the leads. Distinctive interference patterns emerge in the two-terminal conductance that manifest unique properties of quantum-ring subbands, including the transition between massless-Dirac and Schrödinger-like behavior for the lowest one. In addition, the dependence of interference effects on the charge carriers' flavor degree of freedom enables use of quantum rings as tunable flavor-filter devices. As one of the most relevant possible sources of nonuniversal effects in experiments, we considered variations in the design of T junctions between the ring and external leads, including their reduced transparency. Such insight is particularly useful to inform proper analysis of features associated with the crossover between Dirac-like and Schrödinger-like behavior expected for the lowest ($n = \pm 1$) ring subbands.

Results presented here could be further applied, or suitably generalized, to study transport through Dirac-ring conductors that are tunnel coupled to leads and therefore do not conserve the charge carriers' flavor degree of freedom. The effect of disorder scattering in ring segments connecting the leads could similarly be investigated. As the recently noted [80] remarkable robustness of persistent currents in Dirac rings against disorder was attributed to special properties of the lowest ring subband, we expect our two-terminal transport results to be similarly robust.

The formalism employed in our paper provides a tool for investigating more broadly the effect of quantum confinement on particles whose dynamics is governed by a Dirac equation. It could be usefully applied to related effective-model descriptions of charge carriers in semimetallic systems such as Weyl [81] and nodal-line [82] semimetals, opening up possibilities to explore quantum-transport effects in these, and similar, topological materials. Another interesting avenue for future studies expanding on our approach is Dirac-electron physics in hybrid structures. Situations of this type have been considered before in tight-binding transport calculations for graphene rings with superconducting leads [83] or subject to electrostatic potentials [84].

ACKNOWLEDGMENTS

L.G. is the grateful recipient of a Victoria University of Wellington Masters by thesis Scholarship. U.Z. thanks P.M.R. Brydon for useful discussions. R.W. appreciates the hospitality of Victoria University of Wellington during research visits while this work was performed, as well as support by the NSF under Grant No. DMR-1310199. Work at Argonne was supported by the U.S. Department of Energy, Office of Science, Basic Energy Sciences, Materials Science and Engineering Division under Contract No. DE-AC02-06CH11357.

APPENDIX A: DETERMINATION OF HARD-WALL-CONFINED QUANTUM-RING BOUND STATES WITH $l = 0$

To simplify the notation, we introduce the dimensionless quantities $\tilde{k} = k/k_\Delta$, $\tilde{E} \equiv E/(\gamma k_\Delta)$, and $\tilde{\Delta}_0 = \Delta_0/(\gamma k_\Delta)$. The energy eigenvalues and corresponding (non-normalized) eigenstates of the Hamiltonian $\mathcal{H}_{\rm 1D}^{(\tau)}$ can then be expressed as

$$\tilde{E}_{k\pm} = \xi\,\tilde{k}^2 \pm \sqrt{\tilde{k}^4 + (\tilde{\Delta}_0 + 1)\tilde{k}^2 + \frac{\tilde{\Delta}_0^2}{4}}\quad , \tag{A1a}$$

$$\Phi_{k\pm}^{(\tau)}(r) = \begin{pmatrix} 1 \\ \pm\tau\,\mathrm{sgn}(k)\,\gamma_{k\pm} \end{pmatrix} e^{ikr}\quad , \tag{A1b}$$

with the abbreviation

$$\gamma_{k\pm} = \sqrt{\frac{\tilde{E}_{k\pm} - (\tilde{\Delta}_0/2) - (1+\xi)\tilde{k}^2}{\tilde{E}_{k\pm} + (\tilde{\Delta}_0/2) + (1-\xi)\tilde{k}^2}}\quad . \tag{A1c}$$

Solutions of the confinement problem (13) with a hard-wall potential (20) are found by forming a general superposition of the possible eigenstates of $\mathcal{H}_{\rm 1D}^{(\tau)}$ with given energy $\tilde{E}$ and imposing hard-wall boundary conditions. Focusing initially on $|\tilde{E}| \geqslant |\tilde{\Delta}_0|/2$, four wave numbers are obtained as roots of the equation $\tilde{E}_{k\pm} = \tilde{E}$. Two of them are real and given by $\pm\tilde{k}$, the other two are imaginary and given by $\pm i\tilde{q}$. We find the explicit

expressions [85]

$$\tilde{k} = \left[\frac{\sqrt{(1+\tilde{\Delta}_0+2\xi\,\tilde{E})^2+(1-\xi^2)\big(4\tilde{E}^2-\tilde{\Delta}_0^2\big)}-(1+\tilde{\Delta}_0+2\xi\,\tilde{E})}{2(1-\xi^2)}\right]^{\frac{1}{2}}, \tag{A2a}$$

$$\tilde{q} = \left[\frac{\sqrt{(1+\tilde{\Delta}_0+2\xi\,\tilde{E})^2+(1-\xi^2)\big(4\tilde{E}^2-\tilde{\Delta}_0^2\big)}+1+\tilde{\Delta}_0+2\xi\,\tilde{E}}{2(1-\xi^2)}\right]^{\frac{1}{2}}. \tag{A2b}$$

The full *Ansatz* for the bound-state wave function is

$$\Phi_0^{(\tau,n)}(r) = c_{1k}^{(\tau,n)}\begin{pmatrix}1\\ \tau\,\gamma_k\end{pmatrix}e^{ikr} + c_{2k}^{(\tau,n)}\begin{pmatrix}1\\ -\tau\,\gamma_k\end{pmatrix}e^{-ikr} + c_{1q}^{(\tau,n)}\begin{pmatrix}\bar{\gamma}_q\\ -i\tau\end{pmatrix}e^{-qr} + c_{2q}^{(\tau,n)}\begin{pmatrix}\bar{\gamma}_q\\ i\tau\end{pmatrix}e^{qr}, \tag{A3}$$

with the parameters

$$\gamma_k = \mathrm{sgn}(\tilde{E})\sqrt{\frac{1+\xi}{1-\xi}}\left[\frac{2\tilde{E}+\xi\,\tilde{\Delta}_0-\sqrt{(1+\tilde{\Delta}_0+2\xi\,\tilde{E})^2+(1-\xi^2)\big(4\tilde{E}^2-\tilde{\Delta}_0^2\big)}+1}{2\tilde{E}+\xi\,\tilde{\Delta}_0+\sqrt{(1+\tilde{\Delta}_0+2\xi\,\tilde{E})^2+(1-\xi^2)\big(4\tilde{E}^2-\tilde{\Delta}_0^2\big)}-1}\right]^{\frac{1}{2}}, \tag{A4a}$$

$$\bar{\gamma}_q = \sqrt{\frac{1-\xi}{1+\xi}}\left[\frac{\sqrt{(1+\tilde{\Delta}_0+2\xi\,\tilde{E})^2+(1-\xi^2)\big(4\tilde{E}^2-\tilde{\Delta}_0^2\big)}+1-2\tilde{E}-\xi\,\tilde{\Delta}_0}{\sqrt{(1+\tilde{\Delta}_0+2\xi\,\tilde{E})^2+(1-\xi^2)\big(4\tilde{E}^2-\tilde{\Delta}_0^2\big)}+1+2\tilde{E}+\xi\,\tilde{\Delta}_0}\right]^{\frac{1}{2}}. \tag{A4b}$$

The secular equation obtained from imposing hard-wall boundary conditions $\Phi_0^{(\tau,n)}(R\pm W/2)=0$ at the inner and outer ring radii is similar to those found in related bound-state problems [21,38]. It can be written in the concise form

$$\gamma_k\,\bar{\gamma}_q = \begin{cases}\tanh(qW/2)\cot(kW/2) & \text{case a,}\\ -\coth(qW/2)\tan(kW/2) & \text{case b,}\end{cases} \tag{A5}$$

where case $\nu=$ a ($\nu=$ b) yields solutions with even (odd) parity associated with eigenvalues $E_0^{(\tau,n_\nu)}$. The corresponding eigenstates can be written as

$$\Phi_0^{(\tau,n_\nu)}(r) = \Phi_{\mathrm{D}}^{(\tau,n_\nu)}(r) + \Phi_{\mathrm{B}}^{(\tau,n_\nu)}(r), \tag{A6}$$

where the contribution labeled D has the form of a standing-wave state for a Dirac particle [60], and the part labeled B is an evanescent correction that incorporates the remote-band contributions [21]. More explicitly, we find

$$\Phi_{\mathrm{D}}^{(\tau,n_{\mathrm{a}})}(r) = \mathcal{N}_{n_{\mathrm{a}}}\begin{pmatrix}\cos\big[k_{n_{\mathrm{a}}}(r-R)\big]\\ \tau\,\gamma_{k_{n_{\mathrm{a}}}}\,i\sin\big[k_{n_{\mathrm{a}}}(r-R)\big]\end{pmatrix}, \tag{A7a}$$

$$\Phi_{\mathrm{B}}^{(\tau,n_{\mathrm{a}})}(r) = -\mathcal{N}_{n_{\mathrm{a}}}\,\gamma_{k_{n_{\mathrm{a}}}}\frac{\sin\big(k_{n_{\mathrm{a}}}W/2\big)}{\sinh\big(q_{n_{\mathrm{a}}}W/2\big)} \times\begin{pmatrix}\bar{\gamma}_{q_{n_{\mathrm{a}}}}\cosh\big[q_{n_{\mathrm{a}}}(r-R)\big]\\ \tau\,i\sinh\big[q_{n_{\mathrm{a}}}(r-R)\big]\end{pmatrix}, \tag{A7b}$$

$$\Phi_{\mathrm{D}}^{(\tau,n_{\mathrm{b}})}(r) = \mathcal{N}_{n_{\mathrm{b}}}\begin{pmatrix}\sin\big[k_{n_{\mathrm{b}}}(r-R)\big]\\ -\tau\,\gamma_{k_{n_{\mathrm{b}}}}\,i\cos\big[k_{n_{\mathrm{b}}}(r-R)\big]\end{pmatrix}, \tag{A7c}$$

$$\Phi_{\mathrm{B}}^{(\tau,n_{\mathrm{b}})}(r) = \mathcal{N}_{n_{\mathrm{b}}}\,\gamma_{k_{n_{\mathrm{b}}}}\frac{\cos\big(k_{n_{\mathrm{b}}}W/2\big)}{\cosh\big(q_{n_{\mathrm{b}}}W/2\big)} \times\begin{pmatrix}\bar{\gamma}_{q_{n_{\mathrm{b}}}}\cosh\big[q_{n_{\mathrm{b}}}(r-R)\big]\\ \tau\,i\sinh\big[q_{n_{\mathrm{b}}}(r-R)\big]\end{pmatrix}, \tag{A7d}$$

where the $\mathcal{N}_{n_\nu}$ denote normalization factors.

Previous results [21,57–60] for Dirac particles with hard-wall mass confinement are reproduced in the limit $\Delta(k)\to\Delta_0$ and $\epsilon(k)\to 0$, which is achieved by taking $k_\Delta\to\infty$ and $\xi\to 0$ in all relevant expressions [86]. In the process, we have $q\to\infty$, $k\to\sqrt{4E^2-\Delta_0^2}/(2\gamma)$, $\gamma_k\to\mathrm{sgn}(E)\sqrt{(2E-\Delta_0)/(2E+\Delta_0)}$, and $\bar{\gamma}_q\to 1$. As a result, the secular equation (A5) simplifies to [21]

$$\gamma_k = \begin{cases}\cot(kW/2) & \text{case a,}\\ -\tan(kW/2) & \text{case b,}\end{cases} \tag{A8}$$

eigenstates are purely of the Dirac-standing-wave form $\Phi_0^{(\tau,n_\nu)}(r)\to\Phi_{\mathrm{D}}^{(\tau,n_\nu)}(r)$, and the normalization factors are given by

$$\mathcal{N}_{n_\nu} = \frac{1}{\sqrt{W}}\left[\frac{E_0^{(\tau,n_\nu)}\big(2E_0^{(\tau,n_\nu)}+\Delta_0\big)}{2\big(E_0^{(\tau,n_\nu)}\big)^2+E_W\,\Delta_0}\right]^{\frac{1}{2}}, \tag{A9}$$

where $E_W\equiv\gamma/W$ is the energy scale associated with size quantization for the confined Dirac particles.

So far, we have considered bound states of ring-confined Dirac particles that are typical standing waves, i.e., are extended in radial direction across the ring. However, it is well known that the presence of a band inversion (signified within our model by $\Delta_0<0$) gives rise to topologically protected states localized at the system boundaries [22,66,87,88], which should also appear in our situation of interest [38]. In fact, our *Ansatz* (A3) applies to energies $|\tilde{E}|<|\tilde{\Delta}_0|/2$ if the replacements

$$k\equiv i\bar{k} \quad\text{and}\quad \gamma_k\equiv i\,\bar{\gamma}_{\bar{k}} \tag{A10}$$

are made, with the real quantities [89]

$$\tilde{\bar{k}} = \left[\frac{1+\tilde{\Delta}_0+2\xi\,\tilde{E}-\sqrt{(1+\tilde{\Delta}_0+2\xi\,\tilde{E})^2+(1-\xi^2)\big(4\tilde{E}^2-\tilde{\Delta}_0^2\big)}}{2(1-\xi^2)}\right]^{\frac{1}{2}}, \tag{A11a}$$

$$\bar{\gamma}_{\bar{k}} = \mathrm{sgn}(\tilde{\Delta}_0)\sqrt{\frac{1+\xi}{1-\xi}}\left[\frac{\sqrt{(1+\tilde{\Delta}_0+2\xi\,\tilde{E})^2+(1-\xi^2)\big(4\tilde{E}^2-\tilde{\Delta}_0^2\big)}-1-2\tilde{E}-\xi\,\tilde{\Delta}_0}{\sqrt{(1+\tilde{\Delta}_0+2\xi\,\tilde{E})^2+(1-\xi^2)\big(4\tilde{E}^2-\tilde{\Delta}_0^2\big)}-1+2\tilde{E}+\xi\,\tilde{\Delta}_0}\right]^{\frac{1}{2}}. \tag{A11b}$$

The secular equation for $|\tilde{E}| < |\tilde{\Delta}_0|/2$ then reads [66]

$$-\bar{\gamma}_{\bar{k}}\,\bar{\gamma}_q = \begin{cases}\tanh(qW/2)\coth(\bar{k}W/2) & \text{case a,}\\ \coth(qW/2)\tanh(\bar{k}W/2) & \text{case b.}\end{cases} \tag{A12}$$

Corresponding eigenstates for the in-gap bound states are obtained by using the expressions from Eq. (A10) in the wave functions shown in Eqs. (A7a)–(A7d). Because of the positivity of its RHS, solutions of Eq. (A12) exist only for $\Delta_0 < 0$, and there can be at most one solution for each case a and b. Figure 10 illustrates the regimes for which two, one, or no bound states have energies within the gap, assuming materials parameters for a 7-nm HgTe quantum well. The boundaries between these regimes in parameter space can be associated

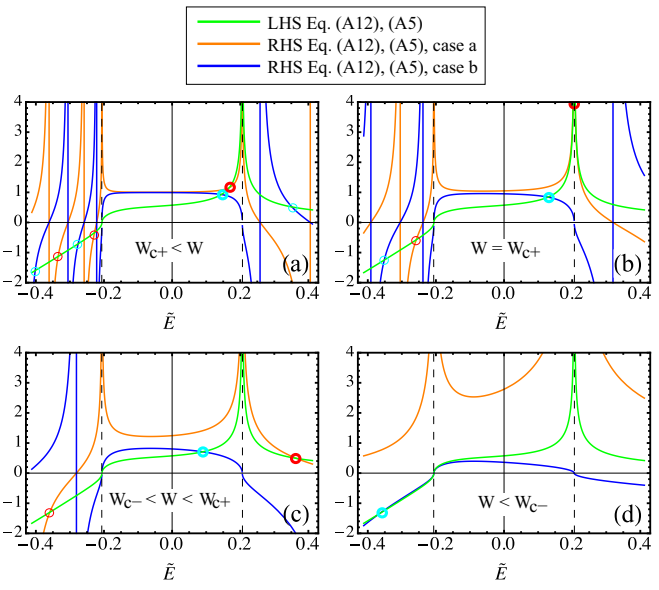

FIG. 10. Ring-confined Dirac-particle states with $l = 0$ related to quantum-spin-Hall edge states. (a) Two bound states with energy inside the gap exist for sufficiently large widths $W_{c+} < W$. (b) When $W = W_{c+}$, one of these states is pushed through the top of the gap. (c) For $W_{c-} < W < W_{c+}$, only one bound-state energy is still within the gap. (d) No bound states exist within the gap for $W < W_{c-}$. In all panels (a) to (d), the LHS expression of the secular equation (A12) [(A5)] is represented by the green curve in the region $|\tilde{E}| < |\tilde{\Delta}_0|/2$ [$|\tilde{E}| > |\tilde{\Delta}_0|/2$], while the RHS for case a (case b) is plotted as the orange (blue) curve. Parameters used are $\tilde{\Delta}_0 = -0.412$, $\xi = 0.746$ (corresponding to a 7-nm HgTe quantum well [65]), and $k_\Delta W = 20$, 13.4, 8, 2.3.

with critical ring widths $W_{c\pm}$. We find analytical expressions in the typical situation where $qW \gg 1$;

$$W_{c\pm} = \lim_{E\to\mp\frac{\Delta_0}{2}}\left\{\frac{2}{\bar{k}}\,\mathrm{arcoth}([\bar{\gamma}_{\bar{k}}\,\bar{\gamma}_q]^{\pm 1})\right\}, \tag{A13a}$$

$$\equiv \frac{2}{|\tilde{\Delta}_0|}\left[\frac{1\mp\xi}{(1\pm\xi)[1+(1\pm\xi)\tilde{\Delta}_0]}\right]^{\frac{1}{2}} k_\Delta^{-1}. \tag{A13b}$$

The critical ring widths arise due to the fact that the size-quantization energy reduces the magnitude of the negative (topological) gap parameter, thereby driving a transition from the topological into the normal regime for the ring band structure that is analogous to similar transitions in higher-dimensional systems [23,67,68]. Note also that, in the limit $W \to \infty$, the secular equations (A12) read $\bar{\gamma}_{\bar{k}}\,\bar{\gamma}_q = -1$, which has the solution [66,90] $\tilde{E} = -\xi\,\tilde{\Delta}_0/2$.

APPENDIX B: DERIVATION OF THE EFFECTIVE DIRAC-RING HAMILTONIAN IN THE $l = 0$-BOUND-STATE BASIS

The azimuthal motion of ring-confined Dirac particles is described by Eq. (16a). Here we analyze the structure of its 2×2 sub-block matrices (16b).

The diagonal blocks having $n = n'$ are Hermitian matrices and can therefore be written as a superposition of Pauli matrices η_j that are acting in the 2×2 subspace spanned by $l = 0$ eigenstates $|\Phi_0^{(\tau,\pm n)}\rangle$,

$$\big(\mathsf{H}_l^{(\tau)}\big)_{n,n} = \sum_{j=0}^{3}\Gamma_j^{(\tau,n)}(l)\;\eta_j \quad . \tag{B1}$$

The most general expression for the coefficients $\Gamma_{lj}^{(\tau,n)}$ are

$$\Gamma_0^{(\tau,n)}(l) = \tfrac{1}{2}\big(E_0^{(\tau,n)}+E_0^{(\tau,-n)}+\big\langle\mathcal{V}_l^{(\tau)}(r)\big\rangle_{n,n}^{(\tau)}+\big\langle\mathcal{V}_l^{(\tau)}(r)\big\rangle_{-n,-n}^{(\tau)}\big), \tag{B2a}$$

$$\Gamma_1^{(\tau,n)}(l) = \Re\mathrm{e}\big\{\big\langle\mathcal{V}_l^{(\tau)}(r)\big\rangle_{n,-n}^{(\tau)}\big\}, \tag{B2b}$$

$$\Gamma_2^{(\tau,n)}(l) = -\Im\mathrm{m}\big\{\big\langle\mathcal{V}_l^{(\tau)}(r)\big\rangle_{n,-n}^{(\tau)}\big\}, \tag{B2c}$$

$$\Gamma_3^{(\tau,n)}(l) = \tfrac{1}{2}\big(E_0^{(\tau,n)}-E_0^{(\tau,-n)}+\big\langle\mathcal{V}_l^{(\tau)}(r)\big\rangle_{n,n}^{(\tau)}-\big\langle\mathcal{V}_l^{(\tau)}(r)\big\rangle_{-n,-n}^{(\tau)}\big). \tag{B2d}$$

These expressions simplify considerably in the electron-hole-symmetric situation $\xi = 0$;

$$\Gamma^{(\tau,n)}_{0,\xi=0}(l) = \gamma\, l\big[\langle\sigma_2/r\rangle^{(\tau)}_{n,n} - \tau\,\langle\sigma_0/(k_\Delta r^2)\rangle^{(\tau)}_{n,n}\big], \quad \text{(B3a)}$$

$$\Gamma^{(\tau,n)}_{1,\xi=0}(l) = \gamma\, l\big[\langle\sigma_0/r\rangle^{(\tau)}_{n,n} - \tau\,\langle\sigma_2/(k_\Delta r^2)\rangle^{(\tau)}_{n,n}\big], \quad \text{(B3b)}$$

$$\Gamma^{(\tau,n)}_{2,\xi=0}(l) = \gamma\, l^2\,\langle\sigma_1/(k_\Delta r^2)\rangle^{(\tau)}_{n,n} \quad , \quad \text{(B3c)}$$

$$\Gamma^{(\tau,n)}_{3,\xi=0}(l) = E^{(\tau,n)}_{0,\xi=0} + \gamma\, l^2\,\langle\sigma_3/(k_\Delta r^2)\rangle^{(\tau)}_{n,n}. \quad \text{(B3d)}$$

Treating the electron-hole-asymmetry contribution $\propto\xi$ in $\mathcal{V}^{(\tau)}_l(r)$ perturbatively, one can approximate $\Gamma^{(\tau,n)}_j(l) \approx \Gamma^{(\tau,n)}_{j,\xi=0}(l) + \delta\Gamma^{(\tau,n)}_j(l)$, with corrections given to first order in small ξ by

$$\delta\Gamma^{(\tau,n)}_0(l) = \xi\left(\partial E^{(\tau,n)}_0/\partial\xi\right)_{\xi=0} + \xi\,\gamma\, l^2\,\langle\sigma_0/(k_\Delta r^2)\rangle^{(\tau)}_{n,n}, \quad \text{(B4a)}$$

$$\delta\Gamma^{(\tau,n)}_1(l) = \xi\,\gamma\, l^2\,\langle\sigma_2/(k_\Delta r^2)\rangle^{(\tau)}_{n,n} \quad , \quad \text{(B4b)}$$

$$\delta\Gamma^{(\tau,n)}_2(l) = \xi\,\gamma\,(-\tau)\, l\,\langle\sigma_1/(k_\Delta r^2)\rangle^{(\tau)}_{n,n} \quad , \quad \text{(B4c)}$$

$$\delta\Gamma^{(\tau,n)}_3(l) = \xi\,\gamma\,(-\tau)\, l\,\langle\sigma_3/(k_\Delta r^2)\rangle^{(\tau)}_{n,n} \quad . \quad \text{(B4d)}$$

Further analysis is facilitated by substituting the eigenstates for a hard-wall mass confinement from Eqs. (A7) as the states between which matrix elements in Eqs. (B3a)–(B3d) and (B4a)–(B4d) are calculated. It is then useful to define the quantities

$$\Xi^{(\tau,n)}_{jm}(W/R) = \langle\sigma_j\,(W/r)^m\rangle^{(\tau)}_{n,n} \quad , \quad \text{(B5)}$$

as these are functions of the ring aspect ratio W/R. The natural energy scale of the $\Gamma^{(\tau,n)}_j(l)$ is then E_W, and terms quadratic in l are suppressed by a factor $1/(k_\Delta W) \ll 1$ typically. From the particular form and r dependence of the spinors in Eqs. (A7), it can be deduced that the leading-order behavior in W/R is $\Xi^{(\tau,n)}_{jm}(W/R) \sim (W/R)^m$ for $j = 0$ and $j = 3$ (i.e., the matrix elements involving diagonal Pauli matrices) whereas $\Xi^{(\tau,n)}_{jm}(W/R) \sim (W/R)^{m+1}$ for $j = 1$ and $j = 2$. Also, the functions $\Xi^{(\tau,n)}_{jm}$ with $j = 0$ and 3 ($j = 1$ and 2) are independent of (proportional to) τ. Finally, $\Xi^{(\tau,n)}_{1m}(W/R) \equiv 0$ identically because the upper (lower) entry in the eigenspinors given by Eqs. (A7) is always real (imaginary). Based on these insights, we parametrize the effective Hamiltonian for azimuthal motion within subbands with labels $\pm n$ in the form given in Eqs. (21), (22a), and (22b).

Taking the limit $W/2 \to R$ in our model yields results that are directly applicable to mass-confined 2D-Dirac electrons in circular quantum dots [91]. However, as W/R is not small in that situation, no hierarchy of magnitudes between matrix elements $(\mathsf{H}^{(\tau)}_l)_{n,n'}$ in Eq. (16a) can be established. Hence, unlike in the case of quantum rings, we cannot obtain a simple effective Hamiltonian that accurately describes the azimuthal motion of 2D-Dirac electrons in a quantum dot.

[1] Edited by V. Fomin, *Physics of Quantum Rings* (Springer, Berlin, 2014).
[2] M. V. Berry, Proc. R. Soc. Lond. A **392**, 45 (1984).
[3] Y. Aharonov and J. Anandan, Phys. Rev. Lett. **58**, 1593 (1987).
[4] Y. Aharonov and D. Bohm, Phys. Rev. **115**, 485 (1959).
[5] Y. Gefen, Y. Imry, and M. Y. Azbel, Phys. Rev. Lett. **52**, 129 (1984).
[6] M. Büttiker, Y. Imry, and M. Y. Azbel, Phys. Rev. A **30**, 1982 (1984).
[7] Y. Aharonov and A. Casher, Phys. Rev. Lett. **53**, 319 (1984).
[8] A. G. Aronov and Y. B. Lyanda-Geller, Phys. Rev. Lett. **70**, 343 (1993).
[9] T.-Z. Qian and Z.-B. Su, Phys. Rev. Lett. **72**, 2311 (1994).
[10] A. A. Kovalev, M. F. Borunda, T. Jungwirth, L. W. Molenkamp, and J. Sinova, Phys. Rev. B **76**, 125307 (2007).
[11] F. Wilczek and A. Zee, Phys. Rev. Lett. **52**, 2111 (1984).
[12] D. P. Arovas and Y. Lyanda-Geller, Phys. Rev. B **57**, 12302 (1998).
[13] M. Büttiker, Y. Imry, R. Landauer, and S. Pinhas, Phys. Rev. B **31**, 6207 (1985).
[14] D. Frustaglia and K. Richter, Phys. Rev. B **69**, 235310 (2004).
[15] M. Pletyukhov and U. Zülicke, Phys. Rev. B **77**, 193304 (2008).
[16] K. S. Novoselov, A. K. Geim, S. V. Morozov, D. Jiang, M. I. Katsnelson, I. V. Grigorieva, S. V. Dubonos, and A. A. Firsov, Nature (London) **438**, 197 (2005).
[17] Y. Zhang, Y.-W. Tan, H. L. Stormer, and P. Kim, Nature (London) **438**, 201 (2005).
[18] A. H. Castro Neto, F. Guinea, N. M. R. Peres, K. S. Novoselov, and A. K. Geim, Rev. Mod. Phys. **81**, 109 (2009).
[19] D. Xiao, G.-B. Liu, W. Feng, X. Xu, and W. Yao, Phys. Rev. Lett. **108**, 196802 (2012).
[20] A. Kormányos, G. Burkard, M. Gmitra, J. Fabian, V. Zólyomi, N. D. Drummond, and V. Fal'ko, 2D Materials **2**, 022001 (2015).
[21] S. R. White and L. J. Sham, Phys. Rev. Lett. **47**, 879 (1981).
[22] B. A. Volkov and O. A. Pankratov, Pis'ma Zh. Eksp. Teor. Fiz. **42**, 145 (1985) [JETP Lett. **42**, 178 (1985)].
[23] B. A. Bernevig, T. L. Hughes, and S. Zhang, Science **314**, 1757 (2006).
[24] M. König, S. Wiedmann, C. Brüne, A. Roth, H. Buhmann, L. W. Molenkamp, X.-L. Qi, and S.-C. Zhang, Science **318**, 766 (2007).
[25] C. Liu, T. L. Hughes, X.-L. Qi, K. Wang, and S.-C. Zhang, Phys. Rev. Lett. **100**, 236601 (2008).
[26] I. Knez, R.-R. Du, and G. Sullivan, Phys. Rev. Lett. **107**, 136603 (2011).
[27] The valley isospin of massless Dirac electrons in graphene constitutes an example for such a flavor quantum number, as does the real spin of charge carriers in a semiconductor quantum well. The two-flavor 2D-Dirac model was originally introduced in the context of quantum field theory [92]. Its application in condensed-matter physics has recently been reviewed in Refs. [64,93].
[28] M. Zarenia, J. M. Pereira, A. Chaves, F. M. Peeters, and G. A. Farias, Phys. Rev. B **81**, 045431 (2010); **82**, 119906(E) (2010).
[29] D. Sticlet, B. Dóra, and J. Cayssol, Phys. Rev. B **88**, 205401 (2013).
[30] N. Bolívar, E. Medina, and B. Berche, Phys. Rev. B **89**, 125413 (2014).

[31] S. Bellucci, A. A. Saharian, and A. K. Grigoryan, Phys. Rev. D **94**, 105007 (2016).
[32] P. Recher, B. Trauzettel, A. Rycerz, Y. M. Blanter, C. W. J. Beenakker, and A. F. Morpurgo, Phys. Rev. B **76**, 235404 (2007).
[33] D. R. da Costa, A. Chaves, M. Zarenia, J. M. Pereira, G. A. Farias, and F. M. Peeters, Phys. Rev. B **89**, 075418 (2014).
[34] J. Wurm, M. Wimmer, H. U. Baranger, and K. Richter, Semicond. Sci. Technol. **25**, 034003 (2010).
[35] J. Schelter, P. Recher, and B. Trauzettel, Solid State Commun. **152**, 1411 (2012).
[36] I. Romanovsky, C. Yannouleas, and U. Landman, Phys. Rev. B **87**, 165431 (2013).
[37] C. González-Santander and F. Domínguez-Adame, Semicond. Sci. Technol. **23**, 125008 (2008).
[38] P. Michetti and P. Recher, Phys. Rev. B **83**, 125420 (2011).
[39] D. Oliveira, J. Fu, L. Villegas-Lelovsky, A. C. Dias, and F. Qu, Phys. Rev. B **93**, 205422 (2016).
[40] M. König, A. Tschetschetkin, E. M. Hankiewicz, J. Sinova, V. Hock, V. Daumer, M. Schäfer, C. R. Becker, H. Buhmann, and L. W. Molenkamp, Phys. Rev. Lett. **96**, 076804 (2006).
[41] S. Russo, J. B. Oostinga, D. Wehenkel, H. B. Heersche, S. S. Sobhani, L. M. K. Vandersypen, and A. F. Morpurgo, Phys. Rev. B **77**, 085413 (2008).
[42] J. S. Yoo, Y. W. Park, V. Skákalová, and S. Roth, Appl. Phys. Lett. **96**, 143112 (2010).
[43] M. Huefner, F. Molitor, A. Jacobsen, A. Pioda, C. Stampfer, K. Ensslin, and T. Ihn, New J. Phys. **12**, 043054 (2010).
[44] D. Smirnov, H. Schmidt, and R. J. Haug, Appl. Phys. Lett. **100**, 203114 (2012).
[45] J. Dauber, M. Oellers, F. Venn, A. Epping, K. Watanabe, T. Taniguchi, F. Hassler, and C. Stampfer, Phys. Rev. B **96**, 205407 (2017).
[46] C. Fan, T. Li, Z. Wei, N. Huo, F. Lu, J. Yang, R. Li, S. Yang, B. Li, W. Hu, and J. Li, Nanoscale **6**, 14652 (2014).
[47] Depending on the physical origin of the flavor degree of freedom in particular materials, *flavortronics* can be synonymous with *valleytronics* [48] (e.g., in graphene) or spintronics [49] (e.g., in semiconductor quantum wells) or a combination of both (e.g., in transition-metal dichalchogenides [50]).
[48] J. R. Schaibley, H. Yu, G. Clark, P. Rivera, J. S. Ross, K. L. Seyler, W. Yao, and X. Xu, Nat. Rev. Mater. **1**, 16055 (2016).
[49] J. Sinova and I. Žutić, Nat. Mater. **11**, 368 (2012).
[50] X. Xu, W. Yao, D. Xiao, and T. F. Heinz, Nat. Phys. **10**, 343 (2014).
[51] The form of the 4×4 Hamiltonian (1a) presumes an appropriate choice of basis functions, and the relation between its diagonal 2×2 blocks (the vanishing of its off-diagonal 2×2 blocks) is due to time-reversal (parity) symmetry. See, e.g., Ref. [94] for a more detailed overview of specific physical realizations.
[52] R. Winkler, *Spin-Orbit Coupling Effects in Two-Dimensional Electron and Hole Systems* (Springer, Berlin, 2003).
[53] Edited by M. Franz and L. Molenkamp, *Topological Insulators* (Elsevier, Amsterdam, 2013).
[54] A. Grüneis, C. Attaccalite, L. Wirtz, H. Shiozawa, R. Saito, T. Pichler, and A. Rubio, Phys. Rev. B **78**, 205425 (2008).
[55] G. Paz, Eur. J. Phys. **22**, 337 (2001).
[56] We follow previous works on ring structures in 2D-Dirac materials [32,38] where a mass confinement embodied by the Lorentz-scalar potential [59] H_V given in Eq. (8) was adopted to simulate confinement realized by lithographic techniques [41–46]. As a possible alternative, a radially symmetric Lorentz-*vector* potential [59]

$$H_U = \begin{pmatrix} U(r)\,\sigma_0 & 0 \\ 0 & U(r)\,\sigma_0 \end{pmatrix}$$

could be considered. Such a potential, which generally arises from electrostatic confinement, was used previously to model gate-defined graphene quantum dots. See, e.g., Refs. [95–97].
[57] M. V. Berry and R. J. Mondragon, Proc. R. Soc. Lond. A **412**, 53 (1987).
[58] B. H. J. McKellar and G. J. Stephenson, Phys. Rev. C **35**, 2262 (1987).
[59] F. A. B. Coutinho, Y. Nogami, and F. M. Toyama, Am. J. Phys. **56**, 904 (1988).
[60] P. Alberto, C. Fiolhais, and V. M. S. Gil, Eur. J. Phys. **17**, 19 (1996).
[61] D. A. Broido and L. J. Sham, Phys. Rev. B **31**, 888 (1985).
[62] S.-R. Eric Yang, D. A. Broido, and L. J. Sham, Phys. Rev. B **32**, 6630 (1985).
[63] States with arbitrary value of l, specifically also $l = 0$, are physical when the quantum ring is connected to leads, which is the situation we are interested in here. In contrast, for an isolated ring, l is required to be *half-integer* for physical states.
[64] R. Winkler and U. Zülicke, ANZIAM J. **57**, 3 (2015).
[65] D. G. Rothe, R. W. Reinthaler, C. X. Liu, L. W. Molenkamp, S. C. Zhang, and E. M. Hankiewicz, New J. Phys. **12**, 065012 (2010).
[66] B. Zhou, H.-Z. Lu, R.-L. Chu, S.-Q. Shen, and Q. Niu, Phys. Rev. Lett. **101**, 246807 (2008).
[67] C.-X. Liu, H. Zhang, B. Yan, X.-L. Qi, T. Frauenheim, X. Dai, Z. Fang, and S.-C. Zhang, Phys. Rev. B **81**, 041307 (2010).
[68] M. Kotulla and U. Zülicke, New J. Phys. **19**, 073025 (2017).
[69] L. Yang, Master's thesis, Victoria University of Wellington, New Zealand, 2017.
[70] This approximation strictly applies only at low temperatures when the Fermi energy in the leads crosses only one of the lowest ($n = \pm 1$) ring subbands. The generalization to multimode configurations that are more realistic when also higher-$|n|$ subbands are populated can be obtained using the approach of Ref. [13].
[71] S. Datta, *Electron Transport in Mesoscopic Systems* (Cambridge University Press, Cambridge, UK, 1995).
[72] For example, the real spin of electrons in graphene is accounted for by $g = 2$.
[73] M. Madou, *Fundamentals of Microfabrication: The Science of Miniaturization*, 2nd ed. (CRC Press, Boca Raton, 2002).
[74] B. Shapiro, Phys. Rev. Lett. **50**, 747 (1983).
[75] T. Itoh, Phys. Rev. B **52**, 1508 (1995).
[76] F. Giazotto, P. Spathis, S. Roddaro, S. Biswas, F. Taddei, M. Governale, and L. Sorba, Nat. Phys. **7**, 857 (2011).
[77] D. Kowal, U. Sivan, O. Entin-Wohlman, and Y. Imry, Phys. Rev. B **42**, 9009 (1990).
[78] P. Földi, B. Molnár, M. G. Benedict, and F. M. Peeters, Phys. Rev. B **71**, 033309 (2005).
[79] U. Aeberhard, K. Wakabayashi, and M. Sigrist, Phys. Rev. B **72**, 075328 (2005).
[80] L. Ying and Y.-C. Lai, Phys. Rev. B **96**, 165407 (2017).
[81] B. Yan and C. Felser, Annu. Rev. Condens. Matter Phys. **8**, 337 (2017).
[82] C. Fang, H. Weng, X. Dai, and Z. Fang, Chin. Phys. B **25**, 117106 (2016).

[83] J. Schelter, B. Trauzettel, and P. Recher, Phys. Rev. Lett. **108**, 106603 (2012).
[84] J. Schelter, D. Bohr, and B. Trauzettel, Phys. Rev. B **81**, 195441 (2010).
[85] The existence of these solutions is guaranteed for any combination of materials parameters as long as $|\xi| < 1$ and $k_\Delta > 0$. These conditions are indeed satisfied for the materials of interest here.
[86] It turns out that both limits $k_\Delta \to \infty$ and $\xi \to 0$ are required to ensure $\bar{\gamma}_q \to 1$. This is an intricacy arising from the well-known [21,98] (and otherwise for our purposes benign) properties of the evanescent 'wing' states with imaginary wave vectors $\pm iq$ in the *Ansatz* (A3). See also Ref. [99] for a related discussion
[87] C. L. Kane and E. J. Mele, Phys. Rev. Lett. **95**, 226801 (2005).
[88] R. Winkler and H. Deshpande, Phys. Rev. B **95**, 235312 (2017).
[89] To exclude situations where $\bar{k}$ and $\bar{\gamma}_{\bar{k}}$ are complex, we assume the condition [38,66] $\tilde{\Delta}_0 > -1/[2(1-\xi^2)]$ to be satisfied.
[90] E. B. Sonin, Phys. Rev. B **82**, 113307 (2010).
[91] A. Gutiérrez-Rubio and T. Stauber, Phys. Rev. B **91**, 165415 (2015).
[92] R. Jackiw and S. Templeton, Phys. Rev. D **23**, 2291 (1981).
[93] V. P. Gusynin, S. G. Sharapov, and J. P. Carbotte, Int. J. Mod. Phys. B **21**, 4611 (2007).
[94] E. A. Fajardo, U. Zülicke, and R. Winkler, Phys. Rev. B **96**, 155304 (2017).
[95] P. G. Silvestrov and K. B. Efetov, Phys. Rev. Lett. **98**, 016802 (2007).
[96] A. Matulis and F. M. Peeters, Phys. Rev. B **77**, 115423 (2008).
[97] P. Recher, J. Nilsson, G. Burkard, and B. Trauzettel, Phys. Rev. B **79**, 085407 (2009).
[98] M. F. H. Schuurmans and G. W. 't Hooft, Phys. Rev. B **31**, 8041 (1985).
[99] P. C. Klipstein, arXiv:1712.01535.